TECHNISCHE HOCHSCHULE LÜBECK

CERN

Department: Applied Natural Sciences
Course: Physical Engineering
Date of submission: 01.07.2021

BACHELOR THESIS

Monte Carlo simulations of light

Estimating and comparing the photon rates of different sources at the Beam Gas Curtain monitor's camera

---

Author:
Noah JENS (291589)

Supervisor:
Kai SEGER

Second supervisor:
Joachim BRUNN

In association with CERN

CERN supervisor:
Marton ADY

CERN-THESIS-2021-082
01/07/2021

Abstract

This thesis aims at giving a rough estimation of the photon rates and with that the ratio of signal to background radiation on the Beam Gas Curtain's camera, an instrument to measure the concentricity and position of the Hollow Electron lens's electron beam relative to the LHC's proton beam, by imaging photons from the spontaneous emission of a neon gas jet, crossing the particle beams.

The Monte Carlo simulation software MolFlow+ and SynRad+ were used to simulate the photons resulting out of the beam-gas interactions, the thermal radiation from the electron gun cathode as well as the synchrotron radiation from the bent proton beam.

The results show a high amount of synchrotron radiation in comparison to the signal originating out of the spontaneous emission of the gas jet, which can threaten the functionality of the BGC and a negligible amount of thermal radiation. At the same time they reveal possibilities for further investigations and improvements to the BGC's design, most importantly, a mask to shield the camera from background radiation.
The main uncertainty of the results lies within the rough approximation of various simulation parameters, as no measured data was available.

Contents

List of Acronyms and Abbreviations

ALICE	A Large Ion Collider Experiment
BGC	Beam Gas Curtain
CAD	Computer-Aided Design
CERN	Conseil Européen pour la Recherche Nucléaire
CMS	Compact Muon Solenoid
HEL	Hollow Electron Lens
HL-LHC	High-Luminosity Large Hadron Collider
IR	Insertion Region
LHC	Large Hadron Collider
LHCb	Large Hadron Collider beauty
RF	Radio Frequency
RR	Roughness Ratio
SE	Spontaneous Emission
SR	Synchrotron Radiation
STL	STereoLitography

List of Symbols

t	Time [s]
dN/dt	Events per second
L	Luminosity [$m^{-2}\,s^{-1}$]
σ	Interaction cross section [m^2]
E	Energy [J]
h	Planck's constant [J s]
ν	Frequency [s^{-1}]
$M_{e,\,\lambda}$	Spectral emittance [$J\,s^{-1}\,m^{-3}$]
c	Speed of light [$m\,s^{-1}$]
λ	Wavelength [m]
k	Boltzmann's constant [$J\,K^{-1}$]
T	Temperature [K], Transmittance
ε_λ	Spectral emissivity
γ	Relativistic factor
p	Pressure [Pa]
V	Volume [m^3]
dN_{real}/dt	Influx rate of real particles/ photons [s^{-1}]
Q	Outgassing parameter [$Pa\,l\,s^{-1}$]
$K_{\frac{real}{virtual}}$	Number of particles/ photons per second each test particle /-photon represents
N	Number of certain quantity
dn	Probability of desorption (Knudsen's cosine law)
ω	Solid angle
θ	Elevation angle
ϕ	Azimuth angle
s	Sticking factor
z	Impingement rate [$s^{-1}\,m^{-2}$]
f	Facet
A	Surface area [m^2]
R	Reflectance
dN_{scaled}/dt	Scaled influx rate of particles/ photons [s^{-1}]
F	Photon flux [s^{-1}]

dl	Step length [m]
I	Beam current [A]
rev_ratio	Revolution ratio
ρ	Radius of curvature [m], Gas jet density [m^3]
P_{tr}	Transmission probability
Z	Photon rate [s^{-1}]
q	Particle charge [C]
d	Gas jet thickness [m]
P	Power [W]
σ_E	Proton beam's energy spread
ε	Geometric emittance [m]
ε_n	Normalized geometric emittance [m]
β	Ratio of proton speed to the speed of light
e	Elementary charge [C]
X	Signal to background ratio

List of Figures

List of Tables

1 Introduction

Particle accelerators are key tools in researching fundamental physics and the development of more advanced accelerators leads to new discoveries, while pushing the boundaries of technology. The biggest and most powerful particle accelerator in the world is the Large Hadron Collider (LHC) at CERN [1]. As part of the High-Luminosity upgrade, which will improve its performance, the collimation system will be supplemented to control halo protons, by passing a hollow electron beam, concentrically around the LHC's proton beam over the course of a few meters [2]. To monitor the transverse cross section of the beams and with that their position as well as concentricity relative to each other, the Beam Gas Curtain instrument is used, which images photons, generated by the interaction of the particle beams and a neon gas jet, transversely crossing the beams [2].

Next to the photons generated by the particle-gas interaction representing the signal, synchrotron radiation from the bend proton beam and thermal radiation originating from an electron-gun cathode, are reflected into the monitors camera, disturbing the measurement. Therefore, an approximation of their magnitude and the ratio of signal to background radiation must be made, identifying potential threats to the functionality of the monitor, while at the same time show possibilities for improving the current design.

This estimation is important, as it creates the opportunity to identify and investigate problems before they arise during measurements and improvements can be made during an earlier design stage of the instrument.

The tool used to calculate the photon rates at the monitor's camera are Monte Carlo simulations, which require a simulation geometry, information about the amount of emitted photons per second and reflective properties of the materials exposed to the radiation.

Due to the lack of measurements regarding simulation properties, rough estimations have to be made, which result in an accuracy in the range of orders of magnitude.

This thesis shows the process of simulating the different light sources along the following structure:

First, a foundation to understand the working principles and relations between the involved instruments and machines is built. Afterwards, the phenomenons resulting in

the emission of light picked up by the camera are explained and an introduction to the software used for the simulations is made.
The successive sections, each present the simulation of a light source in the system, from building the simulation geometry, to estimating the simulation properties.
Finally, the simulation results are presented, before a discussion of limitations, errors and recommendations is made, leading to the conclusion, which summarizes the findings.

2 Theoretical background

In the upcoming sections, information about fundamental aspects of the project will be presented, following these main topics:

- Basic overview over the High-Luminosity Large Hadron Collider upgrade and the involved instruments.
- Principles of photon emission relevant for the simulations.
- The software used in this project.

2.1 Large Hadron Collider

Particle accelerators are crucial to research in fundamental physics. By colliding or annihilating particles, physicists are able to gain insight to the structure and properties of the building blocks of matter and the forces that act upon them. With increasing collision energy, hard to obtain effects can be observed; therefore building more powerful accelerators is bound to progress in fundamental physics [3].

The Large Hadron Collider (LHC) accelerates protons[1], as well as heavy ions and is with 26.7 km circumference and a maximum center-of-mass collision energy of 14 TeV the biggest and most powerful particle accelerator in the world. The ring has eight straight sections called insertion regions (IR) (Figure 1), which alternate with curved sections, containing superconducting dipole magnets to alter the beams trajectory and keep it on the curved path. [1, 4]

[1]Due to the focus on protons in this thesis, they will exclusively be referred to in the following.

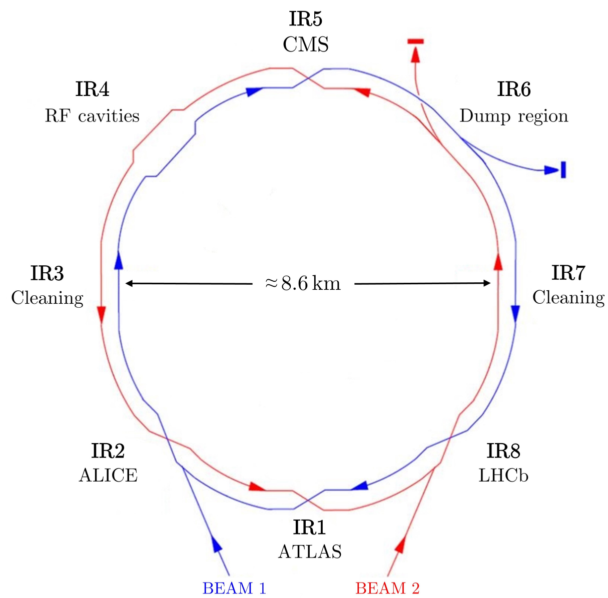

Figure 1: Large Hadron Collider schematic layout, modified based on Figure 1 of [4].

The protons are pre-accelerated in the injector chain of CERN's complex, consistently gathering energy in a series of lower energy accelerators. After injection into the LHC, two proton beams are stored in separate, evacuated beam lines; one turning clockwise (beam 1) and the other one counterclockwise (beam 2). Four of the long straight sections house instruments like the radio frequency cavities, which accelerate the protons to the desired energy, collimator systems that clean the beam to ensure safety by removing particles that stray from the nominal trajectory and a dump region, that removes the beam in case abnormal conditions are detected. [4]
In the remaining four insertion regions, at the main experiments of the LHC, the highly focused proton beams are brought into collision. The two general-purpose detectors Compact Muon Solenoid (CMS) and ATLAS are measuring the collision debris in form of newly generated particles and photons. They consist of several concentric layers of detectors, each optimized for a different kind of measurement to record trajectory, momentum and energy of almost every particle formed. [5, 6]
The ALICE (A Large Ion Collider Experiment) detector is specialized on collisions of lead-ions and studies the properties of a phase with extreme energy density called quark-gluon-plasma. [7]
The Large Hadron Collider beauty (LHCb) experiment is comparing the decays of beauty-quarks and their antimatter counterparts, to find asymmetries and therefore

gain insight on the imbalance, regarding the amount of matter and antimatter in our universe. [8]

The most relevant contribution to fundamental physics of the LHC is the observation of the Higgs boson in the ATLAS and CMS detectors in 2012. It is a particle predicted by the standard model[2] and a manifestation of the Brout-Englert-Higgs mechanism; a theory which “contributes to the understanding of the origin of mass of subatomic particles” [10].

2.1.1 High-Luminosity Large Hadron Collider

In 2013 the CERN council stated “the exploitation of the full potential of the LHC" [11] as the top priority of the European strategy for particle physics. Part of this process is the High-Luminosity LHC upgrade (HL-LHC), allowing further studies of the Higgs boson and physics beyond the standard model [11].
All of the equipment needed for the High-Luminosity upgrade will be installed during the long shutdown 3, between 2025 and mid-2027, before the HL-LHC will be operational at the end of 2027 [12].

Luminosity is a key performance indicator of a particle accelerator, since it determines the collision rate. It can be expressed as the proportionality factor between the events per second dN/dt and the interaction cross section[3] σ: [13]

$$\frac{dN}{dt} = L \cdot \sigma$$

With L in $\mathrm{m}^{-2}\,\mathrm{s}^{-1}$.

In a particle accelerator the probability of observing a process of interest is small and an increase in both peak- and integrated luminosity[4] is desirable, since the detectors are able to gain more data.
The goal of the HL-LHC upgrade is an increase of the instantaneous collision rate by

[2] A theory developed in the early 1970’s, which encapsulates the relations of fundamental particles and the forces that govern them [9].
[3] A measurement of the probability a specific event will occur, in this case a proton-proton collision.
[4] The integral of the luminosity with respect to time.

a factor of 5 and an integrated luminosity gain by a factor of 10 (both with respect to the nominal LHC design values). To meet these goals, the proton beam needs to carry more current and be more focused than in the current LHC system. [14]

Hollow Electron Lens (HEL)

As the number of protons stored in the beam rises with the High-Luminosity upgrade, additional precautions have to be taken to ensure the LHC's safety, since tiny fractions of the stored beam are enough to destroy parts of the accelerator or quench[5] the superconducting magnets. This includes supplementing the existing collimation system with the Hollow Electron Lens (IR4); an instrument to handle beam tails and halo protons (Figure 2) in a more controlled way. [16]

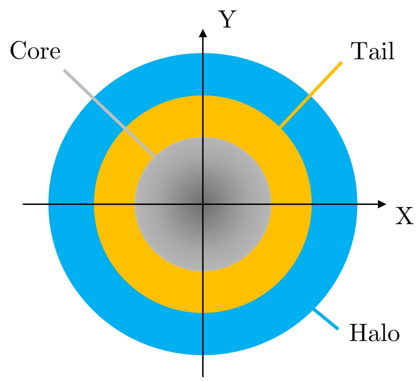

Figure 2: Schematics of the proton beam's transverse profile.

The collimators currently installed in the LHC use a three stage system of ring jaws, which define aperture restrictions for the beam and intercept particles on large amplitude trajectories.

The Hollow Electron Lens (HEL) uses a pulsed electron beam with a hollow current-density profile, which opposes the proton beam and encapsulates it (Figure 3) over the course of a few meters. If the distribution of the electrons is radially symmetrical, the core of the proton beam is unperturbed and only the outer particles receive a non-linear transverse kick due to the opposing electrical charges of the beams, sending the halo protons into the collimators for absorption (Figure 4).

[5]The transition of a superconducting magnet into a resistive state during operation [15].

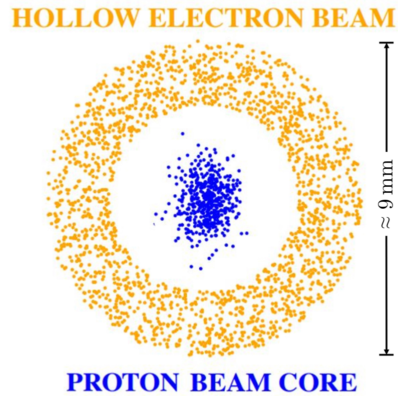

Figure 3: Position of electron lens (orange) and proton beam core (blue) relative to each other. Redrawn from [17].

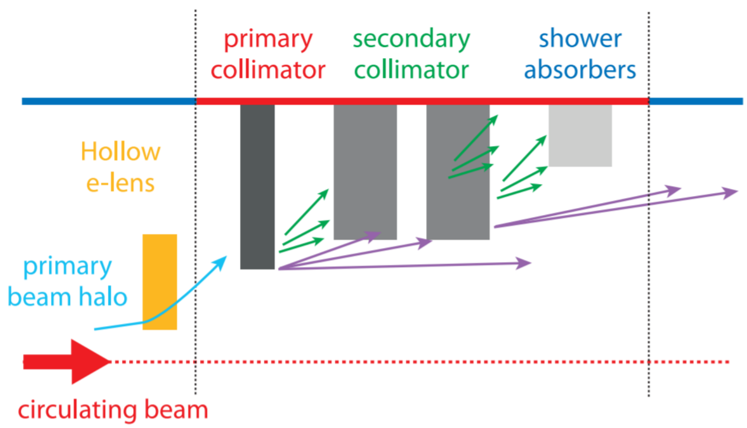

Figure 4: Schematics of halo control with the Hollow Electron Lens [18].

Tuning the parameters of the electron beam allows a smooth and adjustable depletion of halo protons, while reducing the impedance[6] as well as loss spikes and decreasing the probability of accidental beam dump. [16]

The electron lens is generated in the electron gun, equipped with a thermionic cathode made out of tungsten and surrounded by two gun solenoids, used to regulate the compression and the path of the electrons. After acceleration towards the anode in an electric field, the path of the electron lens is bent by the superconducting bending solenoid, injecting it into the LHC beam pipe. The superconducting main solenoids

[6]Interaction between proton beam and vacuum chamber surroundings via electro-magnetic fields [19].

guide the electrons and ensure an overlap of about 3 meters, before the electron lens is ejected from the beam pipe and absorbed by the collector (Figure 5). [16, 20]

Beam Gas Curtain (BGC)

The Beam Gas Curtain (BGC) is a beam profile monitor, to be installed between the two main solenoid cryostats of the Hollow Electron Lens (Figure 5). It allows the observation of the proton beam's and electron lens's transverse cross section as well as their concentricity during operation of the LHC, by imaging photons, which are generated by the interaction of the particle beams and a thin, supersonic neon gas jet (tilted 45° with respect to the beam axis). [2]

The BGC monitor is designed to be minimally invasive with no wearing parts like wires or screens and take measurements in close proximity to the strong magnetic fields of the HEL solenoids [21].

It contains the following main components (Figure 6) [2]:

- **Gas generation stage:**
  A nozzle, followed by skimmers to select and shape the gas jet.

- **Interaction chamber:**
  Interaction point between the particle beams and the gas jet.

- **Exhaust chamber:**
  Pumps residual gas jet and contains diagnostic tools.

- **Optical system:**
  Processes photons and generates the image of the proton beam's and electron lens's transverse cross section.

After passing a 25 mm ⌀ iris, the emitted photons are refracted by a lens system and focused onto the photocathode of an image intensifier where the signal is amplified, before it is picked up by a CMOS camera. This way the setup is able to detect single photons with a quantum efficiency[7] of about 10 % at the wavelength of interest, which is set by a filter between the lens system and the image intensifier. [23]

[7]Ratio of emitted electrons of photocathode to incident photons on it [22].

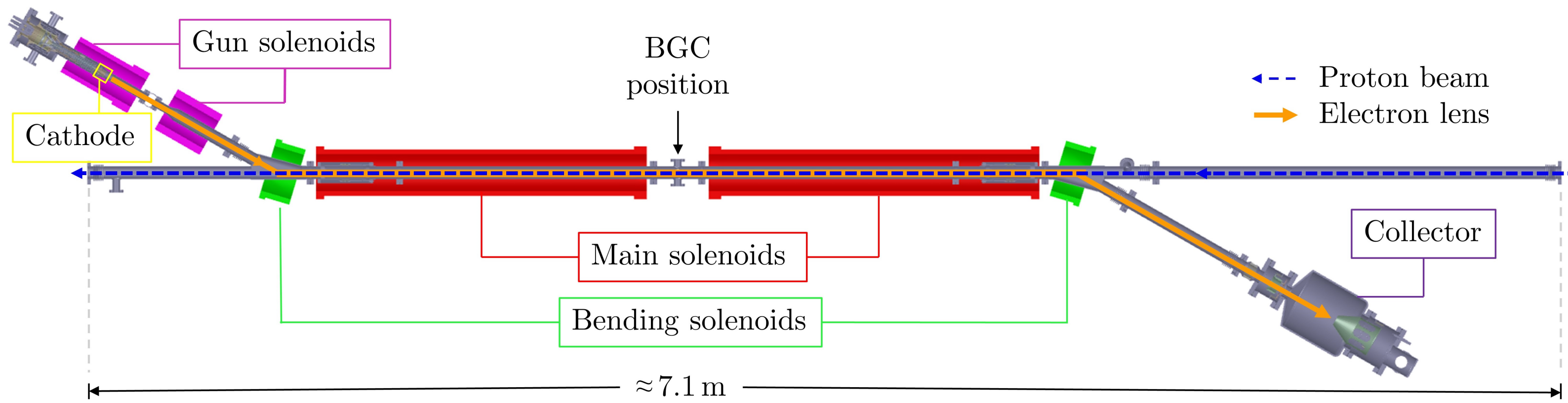

Figure 5: Schematics of the HEL with the main components.

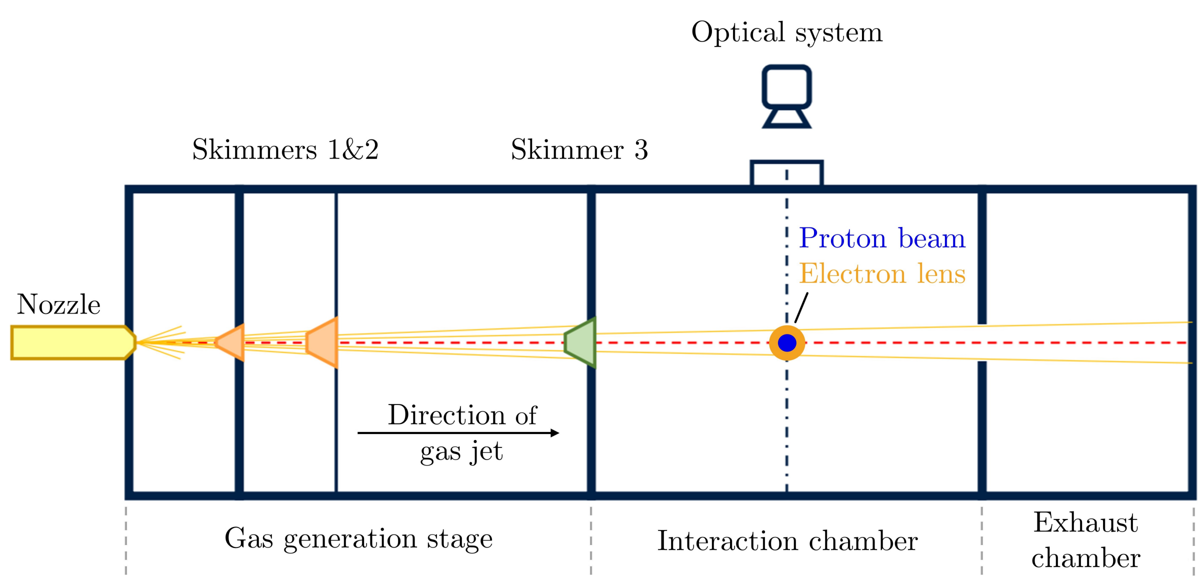

Figure 6: BGC schematics, direction of gas jet perpendicular to the direction of the proton beam and electron lens. Redrawn from [21].

2.2 Excitation of atoms and spontaneous emission of light

To understand and calculate the properties of matter on atomic scale, different models representing the atoms real behavior have been developed. The Bohr model[8] considered a quantum physical approach, thus explaining the hydrogen atom's quantized absorption and emission of electromagnetic radiation [24]. Although there are modern models superior to it, the simplicity and accurate results for selected systems like the hydrogen atom justify taking a closer look at it.

According to the first of two postulates Bohr proposed, electrons are only allowed to orbit the nucleus at discrete distances where their angular momentum is an integer multiple of the reduced Planck constant.
With the second postulate Bohr claimed that every orbit corresponds to an energy state and the transition from an orbit further away from the nucleus to a closer one is connected to the emission of a photon. Further, the photons energy E_{ph} is quantized and dependent on the energy difference of the two involved states: [24, 25]

$$E_{ph} = E_m - E_n = h\,\nu \qquad \text{with} \;\; m > n$$

Where E_{ph} is the photons energy, E_m the higher states energy, E_n the lower states energy, h Planck's constant and ν the photons frequency.

The lowest energy level of an atom is called the ground state. In order to put it in an excited state, where an electron is in a higher orbit, there has to be some energy transfer to it. This can be achieved in different ways, for example by the absorption of electro-magnetic radiation or an inelastic collision [26]. Since the ground state is the most desirable, after a certain lifetime the electron transitions back without any external influence. This process is called spontaneous emission.

2.3 Thermal radiation

As a consequence of the third law of thermodynamics, a temperature of absolute zero is unattainable [27]. Since temperature is a measurement of kinetic energy, the atoms or molecules of a body are always in random motion. This movement includes charged

[8]Developed 1913 by Niels Bohr, basing on a model presented by Ernest Rutherford in 1911.

particles and their acceleration leads to the emission of electromagnetic waves, known as thermal radiation. Its power is dependent on the bodies' temperature, surface and wavelength of emission. [28]
An idealized body, which has the highest spectral radiance and absorbs all incoming radiation, independent from the wavelength and transforms it into heat, is called a black body. [29]

As a form of Planck's law, the spectral emittance of a black body is describing its emitted power per surface area and wavelength:

$$M^b_{e,\lambda}(\lambda, T) = \frac{2\pi hc^2}{\lambda^5} \cdot \frac{1}{e^{\frac{hc}{\lambda kT}} - 1} \tag{1}$$

Where h is Planck's constant, c the speed of light, λ the wavelength of emission, k Boltzmann's constant and T the bodies' temperature. The unit of $M^b_{e,\lambda}$ is $\mathrm{J\,s^{-1}\,m^{-2}\,m^{-1}}$. When plotting the spectral emittance against the wavelength, the emitted spectrum of black body radiation is displayed (Figure 7). [30]

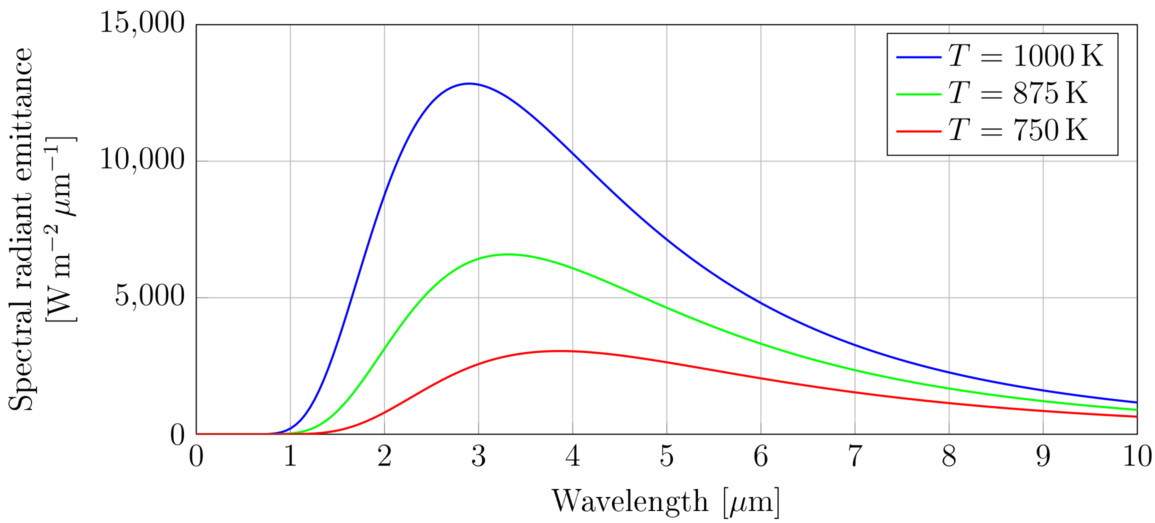

Figure 7: Example of temperature dependent spectrum of black body radiation.

The emissivity ε and absorptivity α are describing the efficiency of emitting (ε) and absorbing (α) radiation. For a black body in thermal equilibrium, they are defined as 1. [29]

A real body only emits part of the black bodies' power and the spectral emissivity ε_λ can be calculated as the ratio of its spectral emittance ($M_{e,\lambda}$) to the one of a black body ($M^b_{e,\lambda}$) at the same temperature: [31]

$$\varepsilon_\lambda(\lambda, T) = \frac{M_{e,\lambda}(\lambda, T)}{M^b_{e,\lambda}(\lambda, T)} \tag{2}$$

2.4 Synchrotron radiation

A charged particle has an electric field surrounding it, with field lines pointing radially towards it (exemplary for negative charge). If the particle is at rest, so is the electric field; the same principle applies for a charged particle in uniform motion. When the charge is accelerated, the information about the change of electric field travels with the speed of light. The field lines close to the source are pointing towards it, but field lines far away still point to the position it was in before acceleration. Consequently, there has to be a regime, where the electric field lines are distorted and this distortion is traveling with the speed of light and can be measured as electromagnetic radiation. [32]

The transverse acceleration in bending magnets of circular particle accelerators leads to emission of electromagnetic waves, which is called synchrotron radiation (SR). Its properties are governed by the relativistic nature of the stored particles. The magnitude is proportional to the particle's charge, acceleration and relativistic factor γ, which is a function of the particle's velocity. Synchrotron radiation is collimated within an angle of $1/\gamma$ and emitted tangentially from any point of the curved path. The light is highly polarized in the direction normal (σ) and parallel (π) to the magnetic field of the bending magnets and its broad spectrum is dependent on the particle's energy and bending radius. [33, 34]

2.5 MolFlow+

If not stated otherwise, the information in the following paragraph and section 2.5.1 is derived from MolFlow+'s documentation [35].

MolFlow+ is a simulation software that was originally developed in the 1990's at CERN to simulate pressure profiles and conductances in an ultra-high vacuum environment,

where the condition of free molecular flow is met. It is based on the Monte Carlo method[9]; a numerical approach, often used for problems that are difficult or impossible to solve analytically.
MolFlow+ launches a certain amount of independent test particles into the system, representing a larger amount of physical ones. The quantities derived from the test particle simulations behave linear and are later scaled up to match the numbers of the physical system.

The following sections will give an introduction into the working principle of MolFlow+ as a vacuum simulation software by guiding you through the cycle of a test particle, explaining selected tools of MolFlow+ as well as addressing the differences between vacuum and light simulations.

2.5.1 Steady-state algorithm

Next to steady-state simulations, where properties like influx rate of gas particles, pumping speed and therefore pressure in the system stay constant, MolFlow+ is able to do time dependent simulations.
The former are used in this project; therefore, further explanations of their working principle will follow, with exception of details only relevant for vacuum simulations.

Facets

The geometric boundaries representing the vacuum system are given by two-dimensional polygons called facets (Figure 8). They are one-sided (if not stated otherwise), thereby only registering hits when a particle arrives from the side the normal vector of the facet points to. A facet has vertices where the edges of the polygon meet and an own local coordinate system. Its u-vector is by default aligned with the longest side of the polygon; the v-vector is orthogonal to it. Both lie in the plane of the facet.

[9]"[S]tochastic simulations [...], that incorporate random variability into the model." [36]

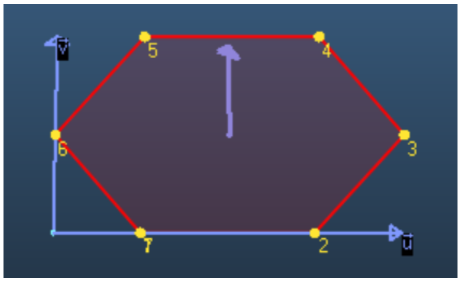

Figure 8: A polygonal facet in MolFlow+ with its vertices (yellow) as well as normal-, u- and v-vector. Tilted view to include normal vector.

Particle generation

MolFlow+ inserts particles into the model via desorbing facets. With the help of the ideal gas equation, the influx rate of physical particles dN_{real}/dt is calculated through an outgassing parameter Q $[\mathrm{mbar\,l\,s^{-1}}]$, which is set by the user:

$$p\,V = N_{real}\,k\,T \tag{3a}$$

$$\frac{dN_{real}}{dt} = \frac{Q}{k\,T} \tag{3b}$$

Where T is the temperature of the facet, which represents the gas source and k is Boltzmann's constant.

The probability of a source facet being selected for desorption is proportional to its influx rate derived above. The position on the facets surface is randomly chosen in a uniform distribution.

Even for low outgassing rates the amount of desorbed particles would be too high to simulate all of them. For that reason one virtual test particle represents a quantity of real particles *per second* according to the following equation:

$$K_{\frac{real}{virtual}} = \frac{\Sigma\, dN_{real}/dt}{N_{virtual}}$$

Where $\Sigma\, dN_{real}/dt$ is the sum of influx rates of all desorbing facets and $N_{virtual}$ is the number of desorbed virtual test particles.

Particle direction

When a particle is generated or reflected off of a wall the direction vector must be determined. In a real system a particle hitting a surface is physi- or chemisorbed by the surface and stays bound to it for a sojourn time. When desorbed again the particle is not affected by its initial momentum anymore and the direction of desorption follows Knudsen's cosine law, where dn is the probability of a particle leaving the surface in solid angle $d\omega$:

$$dn = d\omega \ \pi \ cos(\theta)$$

With θ describing the elevation angle between the particle's direction vector and the facets normal, generated by the following equation:

$$\theta = arcsin(\sqrt{rnd})$$

Where rnd is a random value between 0 and 1.

The azimuth angle ϕ describes the angle between the particle's direction vector and the facets u-vector, lies in the surface's plane and is a random value between 0 and 2π.

Particle speed

The steady-state mode is based on the state of equilibrium, where the amount of particles in the system stays constant and time is defined over the particle influx rate dN_{real}/dt.

Keeping track of particle speeds opens up the possibility to calculate the pressure on a facet based on the particle momentum change. But quantities bound to the momentum of particles are irrelevant in light simulations; therefore, particle speed will not be further examined.

Collision location

The mean free path of a particle describes the distance it travels before an interparticle collision changes its properties like direction or energy. With decreasing particle density the mean free path increases and at some point reaches a regime, called free molecular flow, where particle collisions can be neglected.

By omitting interparticle collisions the only obstacles for a particle are the facets, representing the physical boundaries of the system. Therefore, the ray tracing algorithm only checks for collisions with the facets and chooses the one with the shortest path as the next collision location.

Particle - facet interaction

Particles enter the system via desorbing facets and leave it through pumping facets, which are given a sticking factor s. This property is a value between 0 and 1, describing the probability of an incoming particle being absorbed. Every time a particle collides with a facet, a random number is generated and compared to the facet's sticking factor. If the number is smaller than s, the particle is removed and a new one is generated at a source facet. If it is bigger than s, the particle is desorbed again with a new direction.

An exception to this reflection mechanism is the Low-flux mode; a further explanation can be found in section 2.5.6.

In both cases presented above the interaction of a particle and a facet is registered as a hit. Every facet counts hits to calculate different properties like pressure, particle density or impingement rate. As already discussed, quantities bound to the particle speed will be disregarded; therefore, the impingement rate z, expressing the amount of particles hitting a facet f per second and surface area, will exclusively be described.

$$z = \frac{dN_{f,real}}{dt} \frac{1}{A} = \frac{N_{f,Hit} \, K_{\frac{real}{virtual}}}{A} \tag{4}$$

Where $N_{f,Hit}$ is the number of test particle hits at the facet f and A the facet's surface area.

2.5.2 Using MolFlow+ for light simulations

Due to the disregard of interparticle collisions and the irrelevance of particle speeds for the calculation of the impingement rate, MolFlow+ is able to simulate photons.

The sticking factor s can be seen as the absorption coefficient; consequently, the reflectance R of a material can be expressed as follows:

$$R = 1 - s \tag{5}$$

A difference in simulating particles and photons is their reflection behavior. While particles are desorbed in a cosine distribution, photons can be reflected in two different ways:

- **Specular:**
  Mirror like reflection, where the photon's incident direction is mirrored with respect to the facets surface.
- **Diffuse:**
  Reflection in many different directions, due to material properties like surface roughness. In MolFlow+ diffuse reflected photons follow Knudsen's cosine law.

The ratio of specular and diffuse reflection can be set by the user.

2.5.3 Profiles and textured facets

As stated in 2.5.1 every facet has an own local coordinate system. A profile splits this facet in 100 slices along its u-vector and samples quantities like impingement rate for each slice. The results can be plotted and show a physical quantity along the facets u-axis.
By splitting the facet into cells along the u- and v-vector, MolFlow+ can sample the impingement rate for every cell.
The results can be visualized with a linear as well as logarithmic color scale or read numerically with the "Texture Plotter" tool.
Profiles and textured facets are important tools for diagnostic purposes.

2.5.4 Structures

Since the ray tracing algorithm checks for collisions with every polygon, the simulation time decreases with an increasing number of facets. MolFlow+ is able to divide the model into several structures, which are connected by link facets. The ray tracing algorithm only checks for collisions within the structure the photon was emitted in. Provided a particle crosses a link facet, the algorithm continues to search for collisions within the newly entered structure. That way the amount of facets, which have to be checked for collisions is reduced; generally resulting in faster simulation times.

2.5.5 Iterative Simulations

Especially in light simulations, where almost every facet has a sticking factor, the gradient of impingement rate throughout the model can be fairly high. If the difference in the impingement rate from point A to B is for example 5 orders of magnitude, statistically, 100,000 test particles have to be injected at A, before 1 reaches point B. To save simulation time a second simulation can be launched, emitting directly from point B.
To do so, there has to be one facet in simulation one, recording information about the amount of photons per second at B and their distribution.

Scaled emission rate
To emit the right amount of photons per second at point B, the emission rate has to be scaled accordingly.

$$\frac{dN_{scaled}}{dt} = \frac{dN_{real}}{dt} \frac{N_{Hits}}{N_{virtual}} \tag{6}$$

Where dN_{real}/dt is the emission rate of the source facet at point A, $N_{virtual}$ is the number of virtual test photons emitted in the first simulation and N_{Hits} is the number of hits at the future source facet of the iterative simulation at point B.

Angle maps
To keep track of the angular distribution at point B, MolFlow+ can record elevation angle θ and azimuth angle ϕ of incoming photons. They are stored in an array called "Angle map", where θ and ϕ are sampled as bins. The resolution and therefore the amount of bins is set by the user.

2.5.6 Low-flux mode

Another method to gain more data on regions with a low impingement rate is the low-flux mode. Instead of eliminating photons at collisions with partially sticking facets, they will always be reflected and their represented photon flux F_{in} reduced according to the reflectance R.

$$F_{out} = R \cdot F_{in}$$

After reflection, the photon's reflected flux F_{out} is its new flux F_{in} for the next collision.

The rest of the incoming flux is registered as absorbed by the facet of reflection.

$$F_{absorbed} = (1 - R) \cdot F_{in}$$

In case of a low-flux simulation, next to the normal Monte Carlo hits MolFlow+ also counts the equivalent hits, describing the amount of hits a facet would receive without enabled low-flux mode. The value is calculated as the sum of F_{in}.

A photon will finally be removed, if the ratio of reduced flux (after multiple reflections) to original flux dN_{real}/dt falls below a cutoff ratio, defined by the user.

2.6 SynRad+

SynRad+ is a software to simulate synchrotron radiation, based on the code of MolFlow+. Therefore, a lot of tools as well as the ray tracing engine work similar, though the generation of photons is quite different. In the following sections, the working principle and selected tools of SynRad+, relevant for the simulations in this project, will be explained. For simplicity, details about the calculations behind the generation of test photons will be left out.

The information in the following sections is derived from SynRad+'s documentation [37], where more explanations can be found.

2.6.1 Particle generation

To generate photons of SR, a magnetic region, which causes the acceleration of the charged particles, has to be defined. In this case, the source of synchrotron radiation is restricted to dipole magnets, therefore the magnetic field inside the region is constant. The beam is considered as a succession of tiny dipoles with the step length dl. For each of these trajectory points the location, curvature and beam direction is calculated, according to the magnetic region. Additionally beam width and divergence is taken into account, in case of a not ideal beam.

For emission of a test photon one trajectory point is chosen randomly. The energy is calculated through a reverse interpolation of a cumulative distribution function, obtained out of the SR spectrum. Vertical and horizontal angle of emission are calculated, then offset by a Gaussian-distribution to account for the divergence.

2.6.2 Photon reflection

In SynRad+ the reflectance R is dependent on the photon's energy and incident angle. To obtain the reflectance the Fresnel formulas were used, after calculation of the refractive index from the atomic scattering factor [37]. With this approach an energy and incident angle dependent reflectance library of common materials was included in SynRad+.

The probability that a reflection is specular is given by the Debye-Waller factor, which is dependent on the photons elevation angle, wavelength and the facet's root mean square surface roughness.
The diffuse part of reflection was modeled in a different way compared to MolFlow+. Since the computational resources necessary to precisely calculate the scattered angles would be too high, an analytic approximation of scattered elevation angle $d\theta = \theta_{out} - \theta_{in}$ and the scattered azimuth angle ϕ has been made. Their distribution in the θ_{out}-ϕ-plane can be described as Gaussian-like, where the width is dependent on the incident angle and roughness ratio.
The roughness ratio (RR) is a geometric parameter set by the user, describing the ratio of root-mean-square surface roughness to auto correlation length[10]. The higher the roughness and with that the roughness ratio, the wider the Gaussian perturbations of θ and ϕ.

2.6.3 Test photons representation of synchrotron radiation flux

Similar to MolFlow+, SynRad+ uses a steady-state algorithm and test photons represent a number of real photons per second.
For the calculation of that ratio three parameters are needed:

[10]"[A]verage distance between consecutive hills or valleys on the surface" [38].

SR flux of a full revolution

The synchrotron radiation flux of a full revolution:

$$F_{full\_rev} = 4.131 \cdot 10^{14}\,\gamma\,I$$

Where γ is the relativistic factor and I is the beam current.

Revolution ratio

The ratio, describing how much every step dl represents of the full revolution:

$$rev\_ratio = dl/(2\,\rho\,\pi)$$

Where ρ is the local radius of curvature.

Number of scans

When a photon has been emitted once from every trajectory point, a full scan is reached. Since the probability of emitting a photon is equal for every trajectory point, in statistical terms we can express a full scan as having an equal amount of test photons and trajectory points. Therefore, we can define the number of scans as follows:

$$N_{scans} = \frac{N_{virtual}}{N_{trajectory\_points}}$$

With these three properties SynRad+'s factor of a virtual photon representing real photon flux can be described:

$$K_{\frac{real}{virtual}} = \frac{rev\_ratio \cdot F_{full\,rev}}{N_{scans}}$$

2.7 OpticsBuilder

The OpticsBuilder is a tool to generate 3D geometries and magnetic regions for SynRad+, by defining a list of accelerator parts and their properties.

The elements positions are defined with a coordinate s, resembling the length along the optimal beam path and an orientation θ describing the beam's tangent vector. Each element has a starting point, a length and an aperture (rectangle, circle or racetrack). Additionally, parameters for defining magnetic regions can be incorporated. These parameters can be inserted manually or read out of a TWISS file, containing information about the dipole bending angle as well as the lattice functions, which describe the beam optics. To calculate the TWISS file a program called MAD-X uses a sequence (ordered collection of machine elements) and the beam properties as input. [39, 40]

3 Simulation of spontaneous emission of neon gas jet

In this section the simulation of spontaneous emission (SE), resulting out of the inelastic collision of proton and electron particle beams with neon gas atoms, is presented.

3.1 Geometry

The simulation geometry can be obtained in different ways:

- Importing a STereoLitography (STL)[11] file from a Computer-Aided Design (CAD) software into MolFlow+, then collapsing[12] it.
- Building a simulation geometry with the tools of MolFlow+.

The model is restricted to parts of the BGC system, since the spontaneous emission is spatially limited to the collision point of particles and gas atoms. Hereafter the term "BGC" refers to the simulation geometry and includes the following parts (Figure 9):

Interaction chamber
Partially amorphous carbon (AC) coated (highlighted part in Figure 10) to enhance stray light absorption; houses the radio frequency (RF) liner as well as the camera background shield.

Radio frequency liner
Perforated copper pipe with AC-coated inside, ensuring low beam impedance (Figure 12).

Camera background shield
Polyteknik coated shield [41], to serve as a black background for image taking.

[11] File format that represents a bodies' surface as a number of triangular facets.
[12] Automatically merge vertices with the same coordinates, coplanar facets (if adjacent and with same properties) and contentious edges in MolFlow+.

Camera arm
Connection between interaction chamber and camera system, consisting of black a PVC bellow and lens tubing, which holds the lens system. The vacuum system is closed with a view-port at the foot of the camera arm.

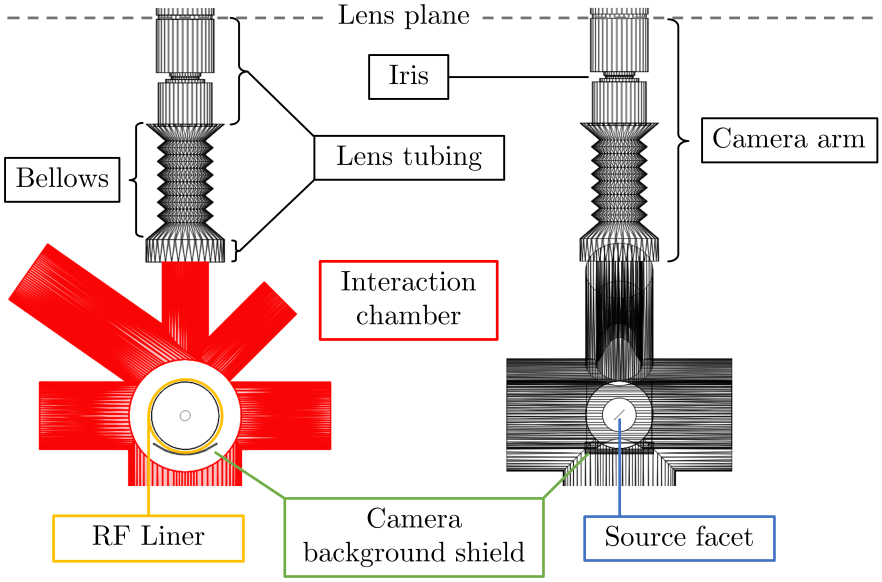

Figure 9: MolFlow+ model of BGC. On the left side the particle beams are going into the plane of the drawing, the right side is rotated 90°. Vacuum pump port under the camera background shield is cut for labeling purposes.

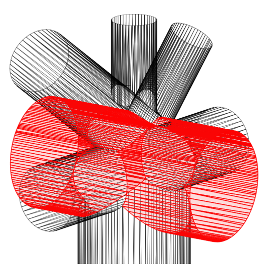

Figure 10: BGC interaction chamber with AC-coating on highlighted parts.

3.1.1 Simplifications

When setting up a simulation geometry, the most intuitive step might be to insert the whole CAD model as a STL file. Unfortunately, this results in a lot of facets, which has negative effects on simulation time. Therefore, a model has to be simplified, which includes finding a compromise between representing the real system and gaining simulation speed.

Interaction chamber and camera arm

The template for building the simulation geometry is given by a CAD file containing the HEL test stand, since it was the latest model of the BGC available. First, the interaction chamber is cut to a length of 200 mm so it fits between the main cryostats of the HEL, then the inner facets are exported and finally measurements of the camera arm are taken to rebuild it in MolFlow+.

The only areas needing simplifications are small features like screw heads, holes, small steps or rounded corners. Since they are not playing a decisive role in the behavior of the system but can use an extensive amount of facets (Figure 11) they have to be simplified. Deleting these features is in general a sufficient method to simplify the model.

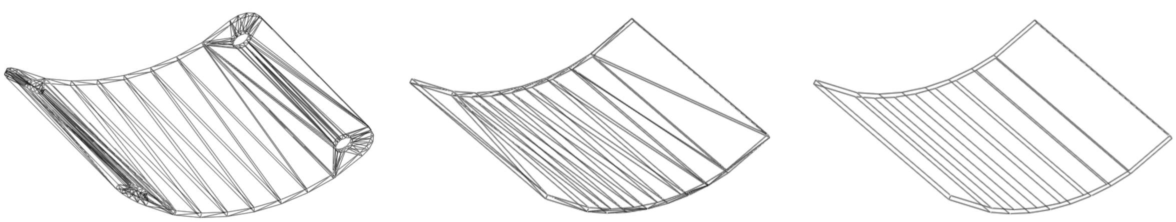

(a) Not simplified: 388 (b) Simplified: 72 (c) Simplified & collapsed: 21

Figure 11: Comparing the number of facets of the camera background shield in different stages of simplification.

Radio frequency liner

The simplification of the RF liner is more complex.

It is positioned inside of the BGC's interaction chamber (Figure 9) and the camera observes the particle-gas interaction through one of the holes in the center of the liner (Figure 12).

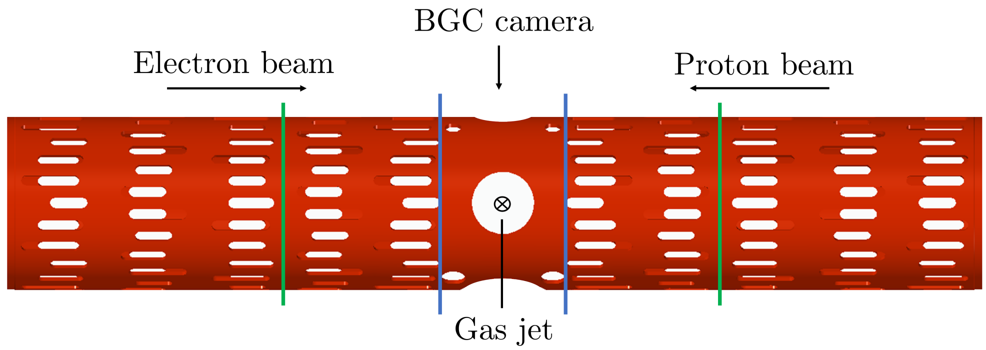

Figure 12: RF liner out of the HEL test stand with direction of electron beam, proton beam, the camera system's optical axis and the gas jet (going into the plane of the drawing). The green lines represent the cuts to shorten the liner, the blue lines indicate the sectioning into three parts, necessary for simplification.

A major difference between the test stand Beam Gas Curtain monitor and the one for the HEL is the diameter of the beam pipes. Thus, the 80 mm diameter test stand liner has to be scaled to 60 mm.
Further, the structure was converted into a cylinder with no wall thickness. To represent the holes, a facet property called "opacity" is used. It is a value between 0 and 1, regulating the transmittance of a facet. An opacity of 0.8 results in reflection or absorption of 80 % of the incoming photons and transmission of 20 %.

As a first step the liner was cut to a length of 200 mm, then divided into three parts (center and two side parts); the position of cuts is marked in Figure 12. As the direct path of light from the source to the camera is going through the center part of the liner it is critical for the following simulations and the pattern of holes was projected onto the cylinder without wall thickness.
For the side parts, the opacity was set according to an approximation of the probability that a photon will completely transmit through one of the holes:

$$P_{tr\_total} = P_{tr\_area} \cdot P_{tr\_hole}$$

Where P_{tr_area} is a geometric factor describing the surface area ratio of holes to full cylinder with the same dimensions and P_{tr_hole} is a factor accounting for the reflection and absorption inside of a hole.

To obtain the latter property a simulation was made, comparing the amount of photons going in and out of a hole.
As the liner has holes in three different sizes, each of them are simulated and the average transmission probability used in (7).
The top and bottom of the hole represent the inside and outside area of the liner. Both have a sticking factor of 1, allowing photons to leave the hole for transmission and reflection back to the origin; only one side is emitting.
The side of the hole, representing the copper material, is assigned a sticking factor according to the reflectance of copper and a ratio of specular and diffuse reflection (values in Table 2, section 3.2.2).
After emission of more than 3 billion test particles per hole, the simulation was stopped and analyzed:

$$
\begin{aligned}
P_{tr\_total} &= P_{tr\_area} \cdot P_{tr\_hole} \\
&\approx 0.272 \cdot 0.815 \\
&\approx 0.222
\end{aligned}
\tag{7}
$$

By subtracting the total transmission probability from 1, the opacity of the side parts is calculated as 0.778.

As mentioned above, the liner inside is AC-coated, meaning that the reflectance of the inside is not the same as for the outside, but even a two-sided facet is not able to represent multiple materials. To resolve this problem the facet's property of being one sided is used, where photons can only interact with the facet from the side its normal vector points to.
In order to model the different materials the simplified liner is inserted twice. One time the facets normal vectors are pointing inwards, one time outwards. This way each side can obtain an independent reflectance (Figure 13).

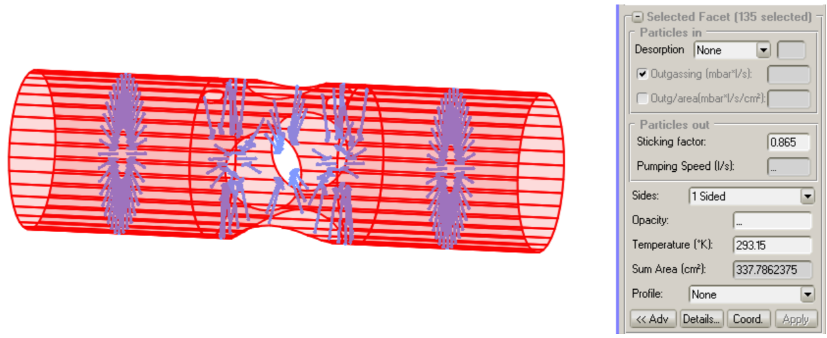

(a) Inside facets, AC-coated, $s = 0.865$

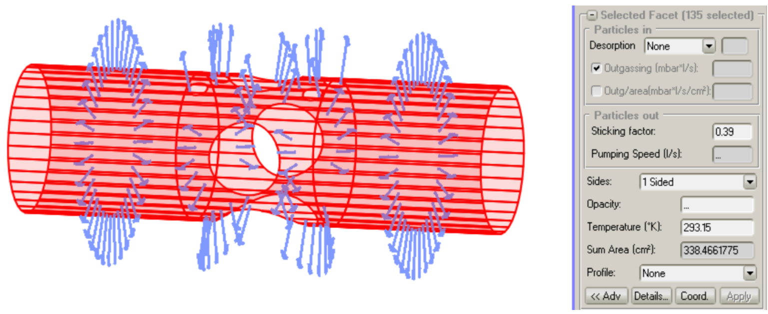

(b) Outside facets, copper, $s = 0.39$

Figure 13: Simplified copper liner with AC-coated inside in MolFlow+.

3.1.2 Source facet

In this case the source facet has to cover the area of particle-gas interaction. Since the majority of photons is emitted by the interaction with the electron lens (Equation 9), all photons are emitted from a single facet, which represents the electron lens's projection onto the tilted gas jet.

This results in an elliptical shape, which shorter axis is with 9 mm [42] as wide as the electron lens and due to the 45° tilt of the gas jet the longer axis of the ellipse has a length of about 12.73 mm.

3.2 Simulation

This section will present the necessary simulation properties and their calculation as well as the method on how to obtain the photon rate of emission.

3.2.1 Emission

The rate of spontaneous emitted photons $Z_{e,\,spont}$ can be calculated with the values in Table 1 and the following equation:

$$Z_{e,\,spont} = I \cdot q^{-1} \cdot d \cdot \rho \cdot \sigma \tag{8}$$

In the Milestone Report 1.1 [43] the excitation cross sections of relativistic protons and non relativistic electrons with the neon gas jet were estimated. These approximations are the base of the following calculations, since no experimental data is available yet. The cross section is dependent on the involved atomic energy states and in this case estimated for the $2p_1 \rightarrow 1s_2$ transition of neon, resulting in the emission of photons with a wavelength of 585 nm [43].
If not stated otherwise the values in Table 1 are taken from this report.

Table 1: Quantities and values to calculate the photon rate of spontaneous emission.

Quantity	Description	Value for protons	Value for electrons
I	Beam current	1.09 A [44]	5.2 A [45]
q	Particle charge	$1.6{\cdot}10^{-19}$ C	$1.6{\cdot}10^{-19}$ C
d	Gas jet thickness	$5{\cdot}10^{-4}$ m	$5{\cdot}10^{-4}$ m
ρ	Gas jet density	$2.5{\cdot}10^{10}$ m^3	$2.5{\cdot}10^{10}$ m^3
σ	Excitation cross section	$4.7{\cdot}10^{-26}$ m^3	$1.4{\cdot}10^{-24}$ m^3

Since the emitted photon rate differs for the proton and electron beam they have to be added to attain the total emitted photon rate $Z_{e,\,spont}$:

$$\begin{aligned} Z_{e,\,spont} &= Z_p + Z_e \\ &\approx 4{\cdot}10^6\, s^{-1} + 5.68{\cdot}10^8\, s^{-1} \\ &\approx 5.72{\cdot}10^8\, s^{-1} \end{aligned} \tag{9}$$

As stated in (3b) the influx rate of real particles or photons dN_{real}/dt is determined by the outgassing parameter Q. To emit photons at the rate of spontaneous emission calculated above, the outgassing parameter of the source facet Q_{spont} has to be set accordingly:

$$
\begin{aligned}
Q_{spont} &= \frac{dN_{real}}{dt}\, k\, T \\
&\approx 5.72 \cdot 10^{8}\,\mathrm{s}^{-1} \,\cdot\, 1.38 \cdot 10^{-23}\,\mathrm{J\,K}^{-1} \,\cdot\, 293.15\,\mathrm{K} \\
&\approx 2.32 \cdot 10^{-12}\,\mathrm{Pa\,m}^{3}\,\mathrm{s}^{-1} \\
&\approx 2.32 \cdot 10^{-11}\,\mathrm{mbar\,l\,s}^{-1}
\end{aligned}
$$

To achieve spherical emission, the source facet must be two-sided and the distribution of emission has to be set to uniform.

3.2.2 Materials and reflectivities

To model the different materials of the BGC components, the facets need to have sticking factors and a ratio of specular and diffuse reflection.
The materials and their reflection properties will shortly be presented in Table 2; further information and references are provided in A.1.

Table 2: BGC components with their materials as well as reflection properties.

Name	Material	Reflectance	Specular	Diffuse
Lens tubing	Black anodized aluminum	1 %	90 %	10 %
Bellow	Black PVC	10 %	80 %	20 %
Interaction chamber	Stainless steel	62.5 %	92.8 %	7.2 %
	AC-coated	13.5 %	80 %	20 %
RF liner	Inside: AC-coated	13.5 %	80 %	20 %
	Outide: Copper	61 %	80 %	20 %
Shield	Polyteknik coated	0.2 %	80 %	20 %

3.2.3 Measurement of photon rate

Due to the low reflectance of the materials in the camera arm, most of the photons reaching the lens plane[13] (Figure 9) have an elevation angle smaller than 11° (Figure 14a).

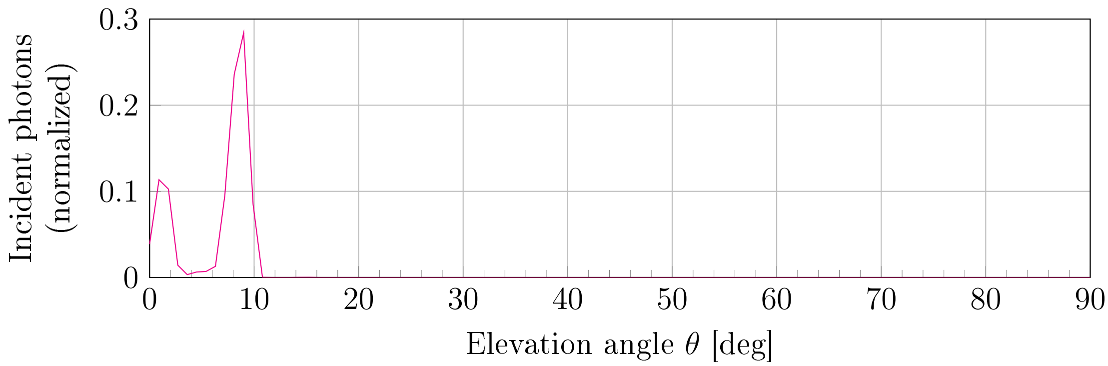

(a) Angular profile of incident photons at the lens plane (normalized).

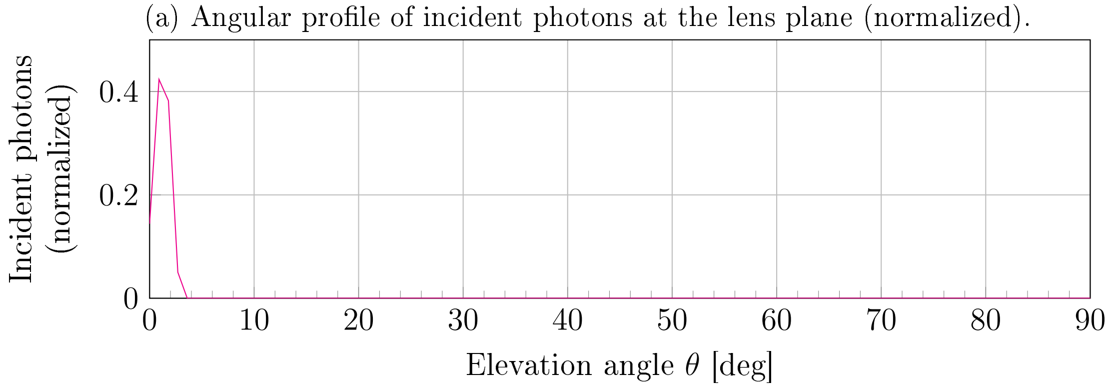

(b) Angular profile of incident photons hitting the lens plane directly (re-normalized).

Figure 14: Angular profile of incident photons at the lens plane, emitted by the gas jet's spontaneous emission.

For that reason the lens system is not accounted for, but it is estimated that the majority of photons reaching the lens plane will be bend onto the photocathode. This way the measurement at the lens plane represents the photon rate at the camera.

[13]Point where the lens system begins.

As MolFlow+ does not directly display the rate of incident photons $Z_{i,\,spont}$ at a facet, it has to be calculated out of the amount of hits and the factor K, describing the photon rate each virtual test particle represents:

$$\begin{aligned} Z_{i,\,spont} &= N_{Hits}\; K_{\frac{real}{virtual}} \\ &= \frac{dN_{real}}{dt}\;\frac{N_{Hits}}{N_{virtual}} \end{aligned} \tag{10}$$

Since the photons, useful for imaging the proton beam and electron lens, are the ones directly hitting the camera, a distinction between direct and indirect hits at the lens plane must be made.

As Figure 14a shows, there are two peaks in the angular profile of incident photons at the lens plane. By running a simulation in which every facet has a sticking factor of 1, only the photons hitting the lens plane directly are recorded (Figure 14b).

When subtracting the photon rate of direct hits from the rate of all incoming photons, the photon rate of indirect hits can be calculated:

$$Z_{i,\,spont}^{indirect} = Z_{i,\,spont} - Z_{i,\,spont}^{direct}$$

4 Simulation of thermal radiation from electron-gun cathode

The thermionic tungsten cathode in the electron gun of the Hollow Electron Lens is emitting thermal radiation at a temperature of about 950 °C [45], which is picked up by the camera system.

The following sections will present the simulation geometry, show the calculation of facet properties and explain the procedure of setting up the necessary simulations.

4.1 Geometry

As the cathode is part of the Hollow Electron Lens system, the geometry generated in 3.1 must be extended.

A model of the HEL was already built for vacuum simulations; to reuse it for the purpose of simulating the cathode's thermal radiation, the BGC model described in 3.1 is inserted (Figure 15a), by connecting the HEL beam pipes with the RF liner.

As the HEL model was originally designed for vacuum simulations with several pump locations, its dimensions are greater and it contains more facets than necessary for the purpose of simulating the cathode's thermal radiation. Therefore, all redundant facets are deleted (Figure 15).

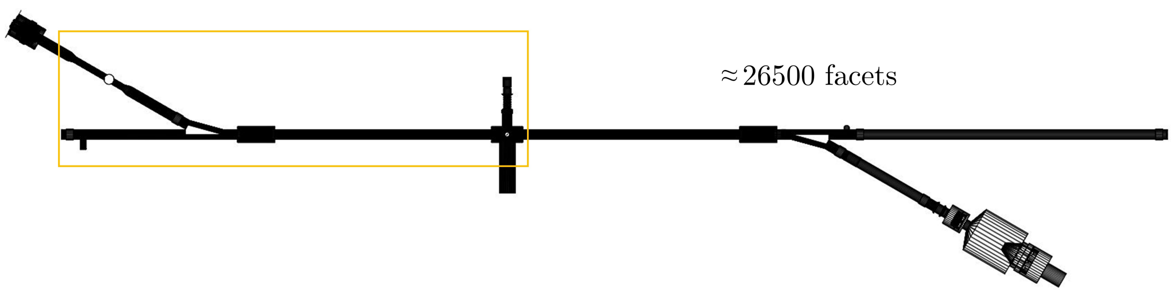

(a) Vacuum simulation model with inserted BGC. Necessary parts for light simulation marked yellow.

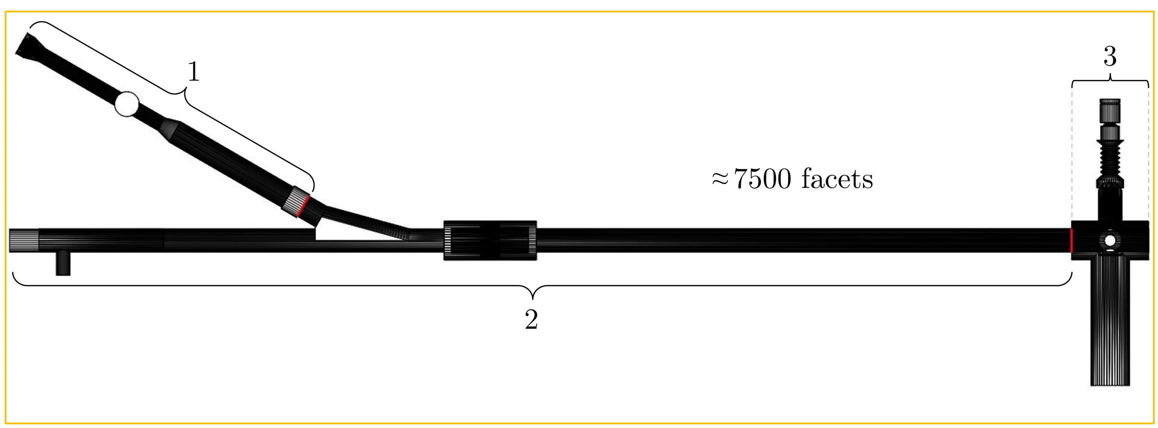

(b) Light simulation model with link facets marked red, dividing the model into three structures.

Figure 15: Comparison of HEL model for vacuum simulations and cathode's thermal radiation simulation.

The facet, which is closing the interaction chamber towards the collector side is assigned a sticking factor, to account for the photons propagating further into the HEL geometry. A test simulation is used to compare the amount of photons going in and out of the interaction chamber's right side. According to this simulation the facet is assigned a sticking factor of 0.985 and diffuse reflection.

Additionally, the light simulation model is divided into three structures (Figure 15b). Combined with the decreasing amount of facets, this results in an improvement of simulation speed (factor of about 8.5)[14].

4.2 Simulation

This section will go over the necessary steps to set up the simulation, including facet properties, their calculation and methods, used to gain more data on low impingement rate areas.

4.2.1 Emission

The ring-shaped cathode is mostly surrounded by other parts and only a fraction of it is pointing towards the direction of the electron's acceleration (Figure 16). If the whole cathode emits photons, the majority of them would spend a disproportionate amount of time bouncing between the cathode's surface and the facets of the parts surrounding it. This occupies a lot of computational power without noteworthy contributing to the photon rate at the lens plane. Therefore, only the part marked red in Figure 16 is set as a source facet, its distribution of emission is approximated as cosine.

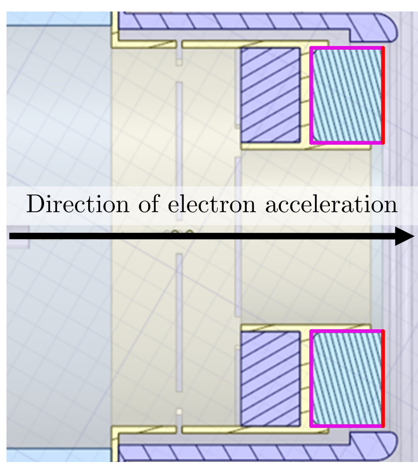

Figure 16: Cross section of the electron gun's cathode (pink) with emitting surface marked red.

[14]Obtained through the ratio of the source facet's desorbed virtual particles per second.

Its photon rate of emission is calculated in three steps:

- Estimate the wavelength range of interest.
- Estimate the power emitted in that wavelength range.
- Divide the power by the photon energy to obtain a photon rate.

The wavelength range of interested is set by the filter in front of the camera, which has its maximum transmittance at the wavelength of spontaneous emission (585 nm) and an approximated bandwidth of 10 nm (Figure 17).

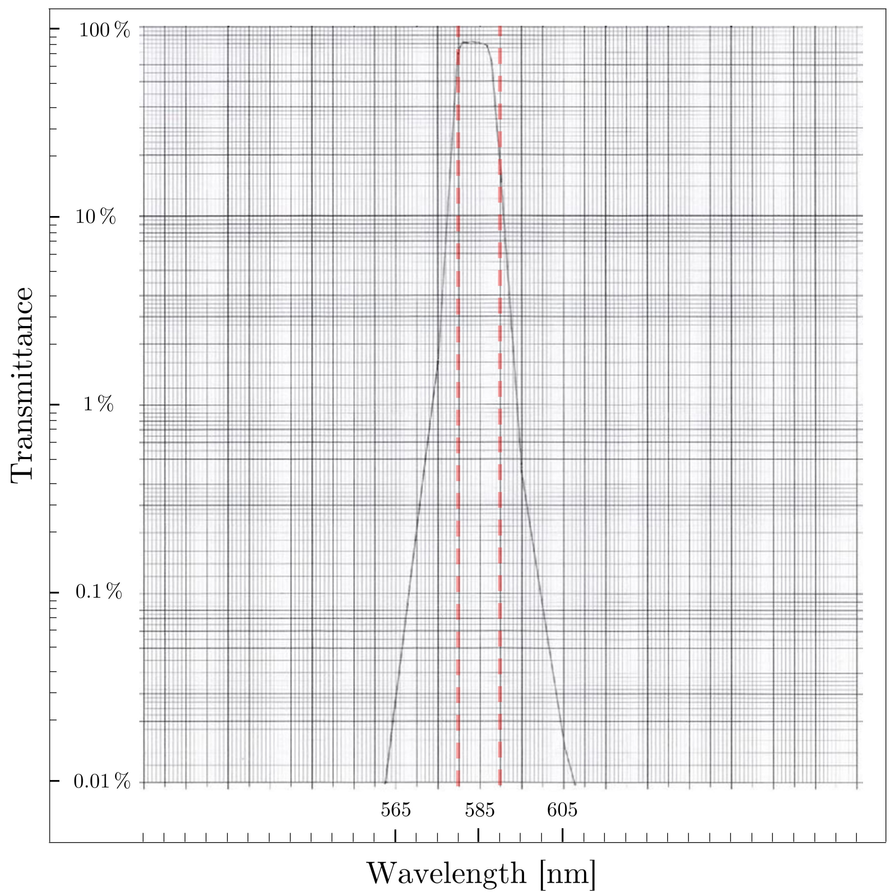

Figure 17: Wavelength dependent transmittance of camera filter with 10 nm bandwidth (marked red) and a maximum transmittance of about 80 %.

As (2) indicates, the cathode's spectral emittance $M_{e,\lambda}$ can be calculated, by multiplying the black bodies' spectral emittance $M^b_{e,\lambda}$ at 950° C (cathode's temperature) [45] with the emissivity of tungsten at 1000 ° C[15] [46]:

$$M_{e,\lambda} = M^b_{e,\lambda} \cdot \varepsilon$$
$$M_{e,\lambda}(\lambda, T) = \frac{2\pi hc^2}{\lambda^5} \cdot \frac{1}{e^{\frac{hc}{\lambda kT}} - 1} \cdot 0.15$$

Due to the small bandwidth, the emitted power ΔP of surface area A in the bandwidth $\Delta\lambda$ can be approximated by isolating the power P out of the of the spectral emittance $M_{e,\lambda}$ [$\mathrm{J\,s^{-1}\,m^3}$]:

$$\begin{aligned} M_{e,\lambda}(\lambda, T) &= \frac{2\pi hc^2}{\lambda^5} \cdot \frac{1}{e^{\frac{hc}{\lambda kT}} - 1} \cdot \varepsilon \\ \frac{\Delta P}{A \cdot \Delta\lambda} &= \frac{2\pi hc^2}{\lambda^5} \cdot \frac{1}{e^{\frac{hc}{\lambda kT}} - 1} \cdot \varepsilon \\ \Delta P &= \frac{2\pi hc^2}{\lambda^5} \cdot \frac{1}{e^{\frac{hc}{\lambda kT}} - 1} \cdot \varepsilon \cdot A \cdot \Delta\lambda \\ \Delta P &\approx \frac{2\pi hc^2}{\lambda^5} \cdot \frac{1}{e^{\frac{hc}{\lambda k \cdot 1223\mathrm{K}}} - 1} \cdot 0.15 \cdot 1.52\mathrm{cm}^2 \cdot 10\mathrm{nm} \\ \Delta P &\approx 2.3\mathrm{mW} \end{aligned} \tag{11}$$

When dividing the emitted power for the cathode's surface area and the wavelength range of interest by the photon energy E_{ph} at 585 nm, an approximation for the photon rate of thermal radiation is found:

$$\begin{aligned} Z_{e,\,therm} &= \frac{\Delta P}{E_{ph}} \\ &= \frac{\Delta P \ \lambda}{h \ c} \\ &\approx \frac{2.301\mathrm{mW} \cdot 585\mathrm{nm}}{h \ c} \\ &\approx 6.78 \cdot 10^{12}\mathrm{s}^{-1} \end{aligned} \tag{12}$$

[15] For unoxidized tungsten, which spectral emissivity is averaged over the whole spectrum [46].

In order to insert it into MolFlow+ the photon rate has to be converted into an outgassing parameter Q_{therm}:

$$Q_{therm} = \frac{dN_{real}}{dt}\, k\, T$$
$$\approx 2.74 \cdot 10^{-7} \mathrm{mbar\, l\, s^{-1}}$$

4.2.2 Materials and reflectivities

If not stated otherwise, all facets that were added in 4.1 have the properties of stainless steel as shown in Table 2.

4.2.3 Iterative simulations

In spite of the simplifications in 4.1, there are no hits at the lens plane (Figure 18) after simulating for more than 16 hours.

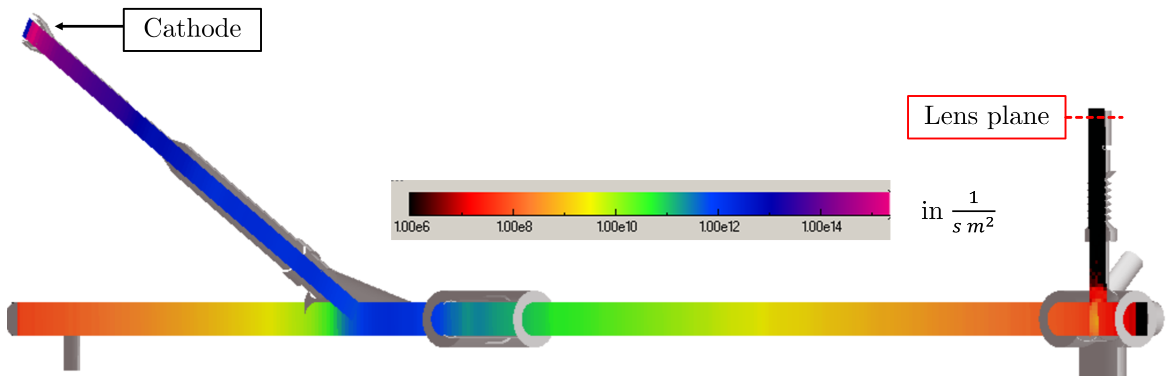

Figure 18: Visualized impingement rate of thermal radiation simulation after about 16 hours of simulation and $8.47 \cdot 10^9$ desorbed virtual photons.

For that reason an iterative simulation is needed; to set it up, several steps are necessary:

- Find location for new source facet.
- Set the resolution and record an angle map.
- Calculate the scaled emission rate.
- Emit from new source facet in second simulation.

To determine the location of the new source facet, the amount of photons at that position is of interest, as more hits allow for a higher angle map resolution and consequently a more accurate simulation. But placing it too close to the original source might not result in the promised gain of simulation speed.
Therefore, a compromise must be found, leading to the least possible amount of iterations while still delivering accurate results in a reasonable amount of time. The chosen facet for the iteration is shown in Figure 19.

Figure 19: MolFlow+ model for simulating cathode's thermal radiation with red marked facet of iteration.

To set the angle map's resolution and with that the number of bins sampling elevation angle θ and azimuth angle ϕ, a test is made with 20 bins sampling θ and 12 bins sampling ϕ (Figure 20).
As shown in Figure 20, the distribution of θ can be approximated as constant over the whole azimuth angle range of 2π. This indicates an independence of the azimuth angle and its resolution can therefore be set to 1.
The resolution of θ can be split into two ranges and as the amount of incident photons drops with $\theta \gtrsim 0.625\,\mathrm{rad}$ this is the point to change resolutions, leading to 100 bins sampling $0\,\mathrm{rad} - 0.625\,\mathrm{rad}$ and 10 bins sampling $0.626\,\mathrm{rad} - \pi/2\,\mathrm{rad}$ (Figure 21).
This provides enough data while maintaining the desired accuracy.

	-2.880	-2.356	-1.833	-1.309	-0.785	-0.262	0.262	0.785	1.309	1.833	2.356	2.880
0.039	3	0	0	3	1	2	4	2	7	2	0	2
0.118	22	82	89	22	22	24	23	24	26	17	19	13
0.196	43	35	22	44	62	84	116	154	165	149	81	73
0.275	319	370	344	302	260	405	934	1028	1062	855	403	266
0.353	1323	1662	1603	1609	1014	805	687	432	404	677	929	1296
0.432	1884	1847	1652	1918	1906	1367	1976	1989	2190	1920	1484	1751
0.511	996	1392	1422	1005	1254	1719	1945	1859	2282	1966	1769	1190
0.589	518	491	472	580	391	359	282	223	197	253	322	378
0.668	63	63	44	63	55	37	50	27	47	44	56	45
0.746	21	18	15	20	21	17	15	20	26	29	20	17
0.825	16	21	14	17	18	13	8	11	13	10	10	17
0.903	14	10	16	14	14	13	18	16	11	15	13	7
0.982	9	7	3	14	5	11	9	7	5	6	5	9
1.060	2	3	6	6	6	6	9	8	6	8	7	12
1.139	7	4	5	4	4	7	6	4	3	4	6	7
1.217	4	7	1	3	4	3	3	5	4	2	1	4
1.296	7	2	3	2	4	0	2	4	4	4	1	2
1.374	4	2	4	1	2	1	5	3	1	1	4	2
1.453	3	1	1	1	0	0	0	1	2	2	2	0
1.532	1	0	0	0	0	0	0	0	0	1	1	0

Figure 20: Thermal radiation angle map test, necessary to set the resolution. Horizontal axis samples ϕ and vertical axis θ, with the axis values representing the center of the bins in rad. Color coded for better visualization.

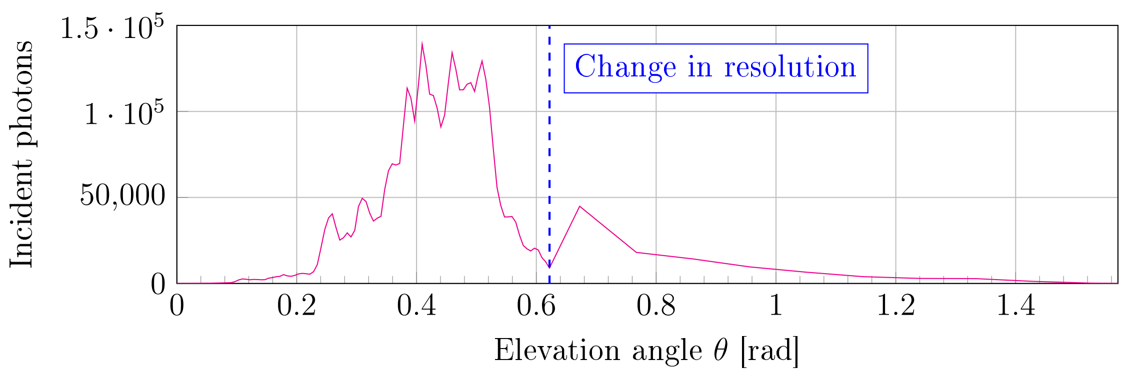

Figure 21: Thermal radiation angle map. Elevation angle θ of 4338946 incident photons sampled over the whole azimuth angle range, with 100 bins from 0 rad $-$ 0.625 rad and 10 bins from 0.626 rad $-$ $\pi/2$ rad.

After the simulation is stopped, the scaled rate of desorption has to be calculated according to (6), with the emitted photon rate of thermal radiation $Z_{e,\,thermal}$ calculated above:

$$\begin{aligned}\frac{dN_{scaled}}{dt} &= Z_{e,\,thermal}\,\frac{N_{Hits}}{N_{virtual}}\\ &\approx 6.78\cdot 10^{12}\mathrm{s}^{-1}\cdot\frac{4.34\cdot 10^{6}}{8.47\cdot 10^{9}}\\ &\approx 3.47\cdot 10^{9}\mathrm{s}^{-1}\end{aligned}$$

To launch the iterative simulation the outgassing parameter $Q_{therm,\,iteration}$ has to be determined:

$$\begin{aligned}Q_{therm,\,iteration} &= \frac{dN_{scaled}}{dt}\,k\,T\\ &\approx 1.41\cdot 10^{-10}\,\mathrm{mbar\,l\,s^{-1}}\end{aligned}$$

Additionally, the recorded angle map must be incorporated as the distribution of emission.

4.2.4 Low-flux iteration

Even though the simulation speed is significantly improved (factor of about 2000)[16] by the iteration, a normal simulation can not deliver enough data at the lens plane facet in a reasonable amount of time.
Activating the low-flux mode allows for more data to be gathered on regions with a low impingement rate.

The only parameter which must be set is the cutoff ratio. Since the difference in impingement rate from source to lens plane is about 7 orders of magnitude, the cutoff ratio is set to $1\cdot 10^{8}$. This way the photons can easier reach the lens plane, without occupying too much computational power by being tracked for too long.

[16] Obtained through the ratio of initial influx rate to the scaled one.

4.2.5 Measurement of photon rate

The photon rate is measured similar to 3.2.3, except the number of Monte Carlo hits N_{Hits} at the lens plane is exchanged for the number of equivalent hits, since the low-flux mode photons only represent a fraction of their initial flux.

5 Simulation of synchrotron radiation

Close to IP4, where the HEL is to be installed, the seperator bending magnets D3 and D4 are widening the distance between the two beam lines (Figure 1, 22). This results in the emission of synchrotron radiation. As the magnet D3 is too close to the BGC, the synchrotron radiation emitted due to its magnetic field travels through the interaction chamber without being reflected onto the lens plane. Therefore, only the synchrotron radiation of D4 will be simulated. To do so, several steps are necessary, which are visualized in Figure 23.

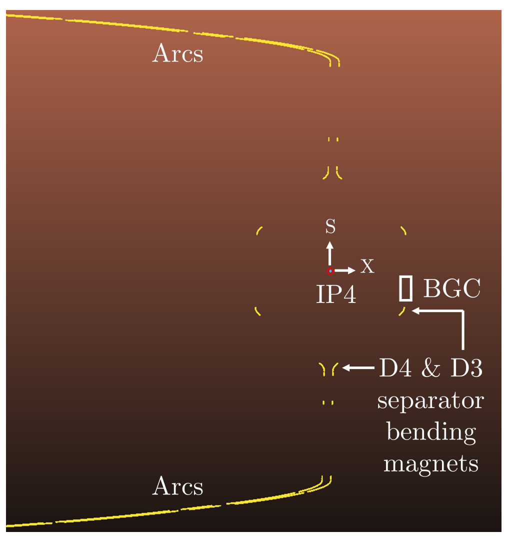

Figure 22: Position of separator bending magnets D3 and D4 as well as the BGC in reference to IP4. Magnetic regions from various magnets visualized in yellow. Redrawn from [41].

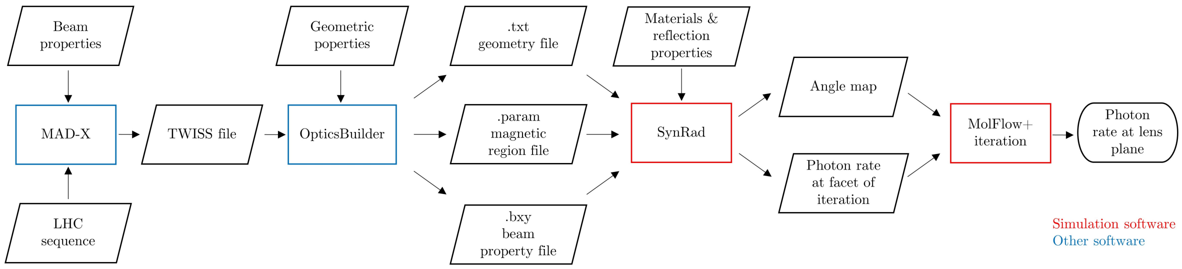

Figure 23: Visualization of the necessary steps to simulate the synchrotron radiation of D4, reaching the BGC camera.

The following section is structured according to the three main software programs used:

- **OpticsBuilder:**
  Generate files necessary for simulation in SynRad+.
- **SynRad+:**
  Simulate synchrotron radiation.
- **MolFlow+:**
  Iterative simulation in MolFlow+.

5.1 OpticsBuilder

In order to start a simulation in SynRad+, three components are necessary:

- **Geometry:**
  A .txt file containing the facets, which represent the vacuum system exposed to synchrotron radiation of D4.
- **Magnetic regions:**
  A .param file describing the magnetic region of the bending magnet D4.
- **Beam properties:**
  A .bxy file containing the beam's energy spread as well as the lattice functions, which describe the beam optics.

Geometry
Out of the LHC aperture graph[17], measurements of the vacuum parts from the bending magnet D4, up to the BGC are taken (about 78 m along the beam path). They can be categorized into three groups:

- **Drift chambers:**
  Cylindrical vacuum chambers without change in aperture.

- **Beam screens:**
  Shield the superconducting magnet cold bores from synchrotron radiation. Perforated to ensure cryo-pumping[18] by the cold bores and copper coated on the inside to minimize beam impedance. [47]

- **Warm modules:**
  Vacuum chambers that establish a connection between parts at cryogenic and room temperature. The RF fingers (marked blue in Figure 24) ensure low beam impedance while being able to handle the thermal expansion of the beam pipes.

In order to generate the warm module geometries with OpticsBuilder, a simplification is necessary, where only the components closest to the beam are modeled (marked red in Figure 24).
For simplicity other parts like gate valves are not included and exchanged for drift chambers. Additionally, the perforation of the beam screens and warm modules is neglected (except for the RF fingers).

According to the LHC aperture graph all changes in aperture and the length between them are incorporated into OpticsBuilder.

[17]Database of LHC components and their apertures.
[18]The sojourn time is temperature dependent and for cryogenic surfaces long enough, that they act like vacuum pumps.

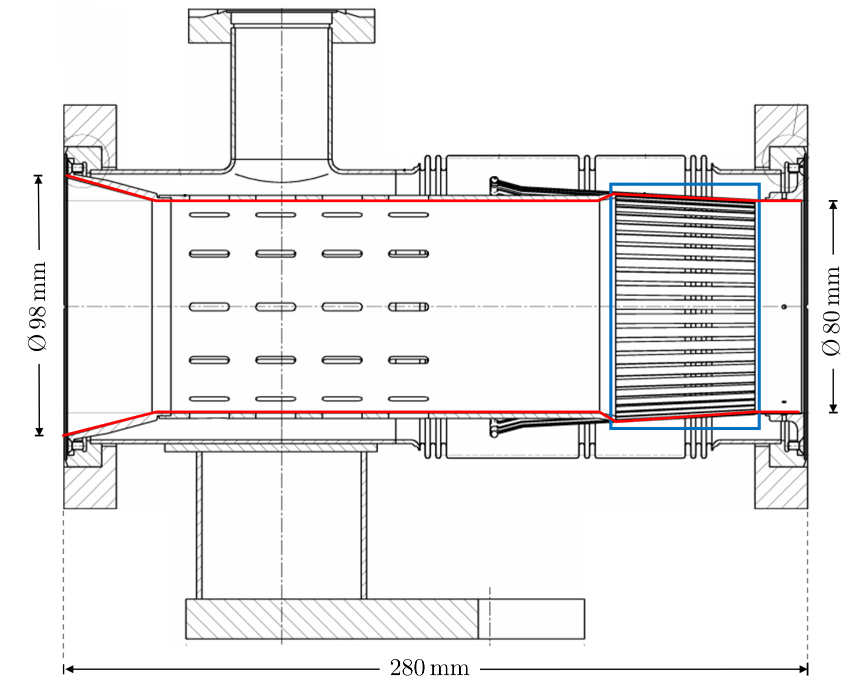

Figure 24: Cross section of warm module example with red outline modeled by Optics-Builder and RF fingers marked blue.

Magnetic regions and beam properties

The properties for the magnetic regions and the proton beam optics are crucial for the simulation. The TWISS file is generated with MAD-X, by using the properties of the High Luminosity LHC beam (Table 3) as well as the LHC sequence between D4 and the BGC.

Table 3: High Luminosity proton beam properties for generating TWISS file. Values from [44].

	Energy	**Beam current**	**Energy spread**	**Emittance X**	**Emittance Y**
Symbol	E	I	$\sigma_E = \Delta E / E$	ε_x	ε_y
Value	7 TeV	1.09 A	$1.13 \cdot 10^{-4}$	$3.351 \cdot 10^{-10}$ m	$3.351 \cdot 10^{-10}$ m

The geometric emittance in X and Y direction $\varepsilon_{x,y}$ has to be calculated out of the normalized emittance ε_n:

$$\begin{aligned}\varepsilon_{x,y} &= \frac{\varepsilon_n}{\beta\,\gamma} \\ &= \frac{2.5\cdot 10^{-6}\,\mathrm{m}}{\beta\,\gamma} \\ &\approx 3.35\cdot 10^{-10}\,\mathrm{m}\end{aligned}$$

With γ as the relativistic factor for the proton beam at 7 TeV and β as the ratio of proton speed to the speed of light.

The properties of the magnetic region as well as the lattice functions for the magnet D4 are copied out of the TWISS file and incorporated into OpticsBuilder.
With these information entered, OpticsBuilder can write the .txt, .param and .bxy files.

5.2 SynRad+

In the following, the simulation of synchrotron radiation in SynRad+ is presented, divided in geometry and simulation properties.

Geometry
As the geometry generated with OpticsBuilder is restricted to the the vacuum parts in front of the BGC, the model is extended with the BGC geometry built in section 3.1 (Figure 25).

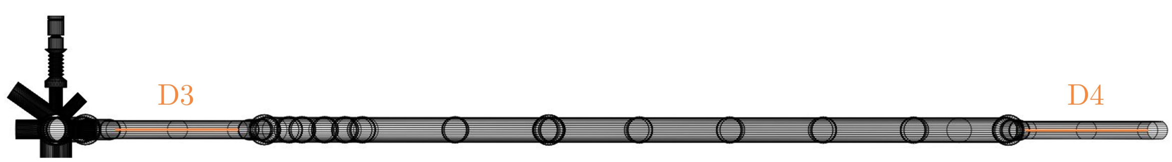

Figure 25: Synchrotron radiation geometry in SynRad+ with magnetic regions of separator bending magnets D3 (not included in the simulation) and D4. Tilted view to picture the whole geometry.

Simulation properties

As mentioned above, the material's reflectivities in SynRad+ are chosen out of a predefined library, including copper for the beam screens and iron as an approximation for stainless steel.

The other materials in the BGC like AC-coating, PVC and anodized aluminum are approximated with a sticking factor, which is not energy and elevation angle dependent. Their values are taken from Table 2.

Additionally the RF fingers of the warm modules are assigned a new material, which is based on iron, but the reflectance is decreased to account for the photons entering the slits. It is estimated, that these photons will not reenter the geometry and therefore can be absorbed.

A new reflectance R_{finger} is calculated for every reflectance R_{iron} in the reflectance table for iron.

$$R_{finger} = \frac{A_{fingers}}{A_{cylinder}} \cdot R_{iron}(\theta,\, E_{ph})$$

With $A_{fingers}$ as the surface area of the RF fingers and $A_{cylinder}$ as the surface area of a full cylinder with the same dimensions.

As the photons of synchrotron radiation have to pass the filter described in 4.2.1, the emission can be restricted to photons in the range of $585\,nm \pm 5\,nm$. To include these boundaries into SynRad+ they have to be converted into photon energy E_{ph} [eV]:

$$E_{ph} = \frac{h\,c}{e\,\lambda}$$

$$E_{min} \approx \frac{h\,c}{e \cdot 590\,\mathrm{nm}} \approx 2.101 \text{ eV}$$

$$E_{max} \approx \frac{h\,c}{e \cdot 580\,\mathrm{nm}} \approx 2.138 \text{ eV}$$

With e as the elementary charge.

The roughness ratio values are based on a previous SynRad+ simulation for the separator bending magnet D4[19]. Figure 26 shows a comparison between a simulation with and without rough surface scattering. The peaks in photon flux are multiple reflections inside of the drift chamber, caused by photons hitting the taper of the warm module on the right side of Figure 26.

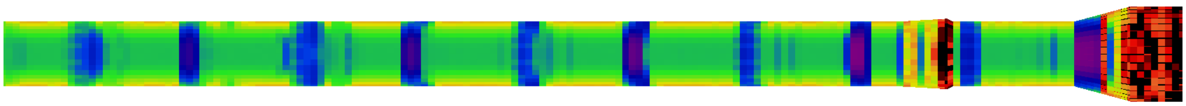

(a) Without rough surface scattering.

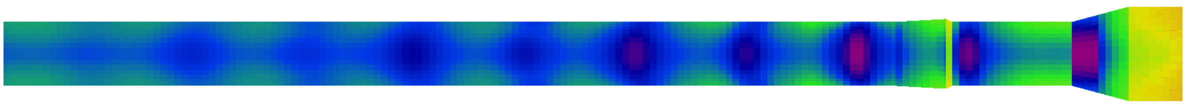

(b) With rough surface scattering (0.001 for stainless steel and 0.0005 for copper).

Figure 26: Example of synchrotron radiation's visualized absorbed and reflected photon flux on warm module and drift chamber, with and without rough surface scattering. Direction of photons from right to left.

Where the simulation with no rough surface scattering has sharp changes in photon flux and irregular artifacts, the simulation with a roughness ratio of 0.0005 for copper and 0.001 for the other materials has a smoother flux distribution, which is closer to what is to be expected of the real system.

Iterative simulation with SynRad+

After running the simulation for multiple days, not enough data could be gathered at the lens plane and even with the low-flux mode enabled, the photon rate does not seem to converge.

Therefore, a method is necessary to use some kind of iterative simulation with SynRad+, since it is not able to record an angle map directly or emit according to it.

The particle logger[20] is used to track the elevation and azimuth angle of incoming photons at the facet of iteration, which is positioned in the interaction chamber's port towards the camera system (subsequently called "steel port") (Figure 28). With an Excel formula, this information is transferred into an angle map, by assigning the 5249

[19]Simulation by Marton Ady, presented in [41].

[20]A tool to track different properties of all incident photons on a chosen facet.

recorded photons to bins. Since the camera arm is radially symmetrical and the azimuth angle distribution at the lens plane is not of interest, the ϕ resolution is set to 1, allowing an elevation angle resolution of 40 bins to be set (Figure 27).

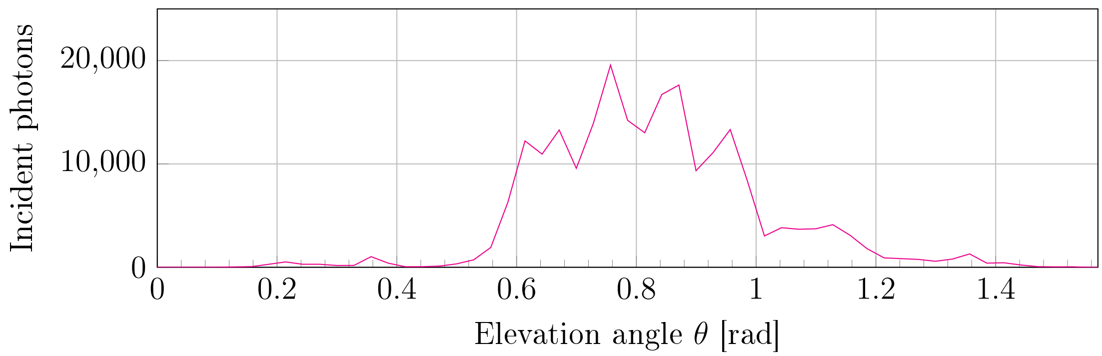

Figure 27: Synchrotron radiation angle map. Elevation angle of 255791 incident photons sampled over the whole azimuth angle range, with 55 bins from 0 rad $-$ $\pi/2$ rad.

In a subsequent MolFlow+ simulation, the photons are emitted according to the angle map recorded in SynRad+.

Since SynRad+ is able to display the photon rate at the facet of iteration $dN_{iteration}/dt$, it can directly be transformed into the outgassing parameter Q_{SR}:

$$\begin{aligned} Q_{SR} &= \frac{dN_{iteration}}{dt}\, k\, T \\ &\approx 3.16 \cdot 10^{9}\,\mathrm{s}^{-1}\, k\, T \\ &\approx 1.28 \cdot 10^{-10}\,\mathrm{mbar\,l\,s}^{-1} \end{aligned}$$

5.3 MolFlow+

In the MolFlow+ simulation, the BGC model of the spontaneous emission (presented in 3.1) is used. The facet of iteration is copied out of SynRad+ and incorporated into the BGC model (Figure 28). Afterwards, the original source facet is deleted and the facet of iteration is assigned the angle map distribution recorded in SynRad+ as well as the outgassing parameter Q_{SR}.

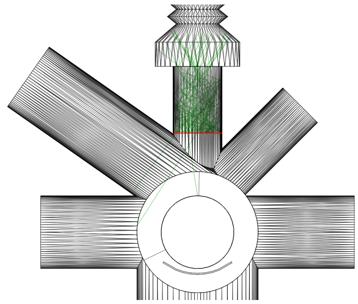

Figure 28: Synchrotron radiation iteration in MolFlow+. The desorbing facet inside of the steel port is marked red and the green lines exemplary represent the trajectory of the emitted test photons.

Apart from the emission, the simulation properties and the method of measurement are the same as in the previous simulations.

6 Results

The photon rates at the lens plane in Table 4 are multiplied with a factor T_{total} to account for the transmittance of the vacuum view-port between the camera arm and the BGC interaction chamber (spectral reflectance shown in Figure 46 in A.2), the lens system [23] and the filter in front of the camera (Figure 17).

$$\begin{aligned} T_{total} &= T_{view-port} \cdot T_{lens-system} \cdot T_{filter} \\ &\approx 0.99 \cdot 0.8 \cdot 0.8 \\ &\approx 0.634 \end{aligned} \tag{13}$$

The scaled results are presented in Table 4 and visualized in Figure 29.

Table 4: Simulation results with the photon rates at the lens plane differentiated according to signal and background; scaled according to the transmittance of the optical system and vacuum view-port.

Simulation	**Photon rate of emission** $[s^{-1}]$	**Photon rate at lens plane** $[s^{-1}]$	
Spontaneous emission	$5.72 \cdot 10^8$	signal	155103
		background	425946
Thermal radiation	$6.78 \cdot 10^{12}$	background	6
Synchrotron radiation	$2.26 \cdot 10^{15}$	background	954202

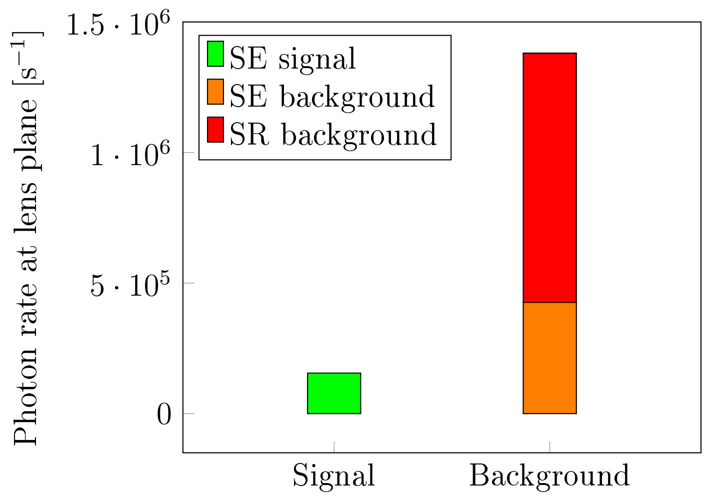

Figure 29: Visualized simulation results.

From Table 4 the ratio of signal to background photons per second X is calculated as follows:

$$X \approx \frac{155103\,\mathrm{s}^{-1}}{425946\,\mathrm{s}^{-1} + 6\,\mathrm{s}^{-1} + 954202\,\mathrm{s}^{-1}}$$
$$\approx 0.11$$

7 Discussion

The results indicate that in the current setup, the amount of background radiation on the BGC monitor's camera might pose a threat to its functionality, as according to the simulations the background photon rate is about nine times as high as the signal's.
Especially the synchrotron radiation can be identified as a problem, since it is the source of background radiation with the highest photon rate at the lens plane and presumably, more invasive changes are necessary to reduce it (more in section 7.6).
The number of photons per second reaching the lens plane, which are emitted by the thermal radiation of the electron gun cathode on the other hand is small in comparison to the other light sources.

In the following sections, the errors in the approximation of simulation properties are estimated and potential improvements are discussed.

7.1 Accuracy of MolFlow+ and SynRad+

As all simulations are made with these programs, their accuracy will be discussed subsequently.

7.1.1 MolFlow+

The steady-state algorithm of MolFlow+ for vacuum simulations has been validated in many occasions in accelerator design since it has been developed [48].

The effects of implementing specular and diffuse reflection to model electro-magnetic waves will be discussed in 7.3.2.

7.1.2 SynRad+

The principle on which the emission of photons in SynRad+ is calculated, is used in different simulation programs [48] and a brief overview of the validation can be found in [49]. A limitation of SynRad+, which lies within the calculation of the emission spectrum, shows with a high photon energy in comparison to the particles energy, as the real synchrotron radiation spectrum is discrete, but approximated as continuous in

SynRad+ [49]. Since the photon energy in section 5.2 is restricted to visible light and the proton beam has an energy of multiple TeV, this limitation is not of concern for the simulation of synchrotron radiation presented above.

The calculation of specular and diffuse reflection in SynRad+ is based on an analytic model described in [50]. Simulations in SynRad+ show a "discrepancy for low grazing angles, most visible for the out-of-plane distribution for 1 and 2 degrees" [48] (the out-of-plane distribution describes the azimuth distribution) in comparison to the analytic model, but a negligible difference for all other incident angles [48].

7.1.3 Converging results

Since Monte Carlo simulations use a numerical approach, the results in MolFlow+ and SynRad+ show a fluctuation during the simulation. With more photons emitted, the magnitude of these fluctuation decreases. The convergence plotter tool can be used to show the evolution of the photon rate at the desired facet over the increasing number of desorptions (Figure 30).

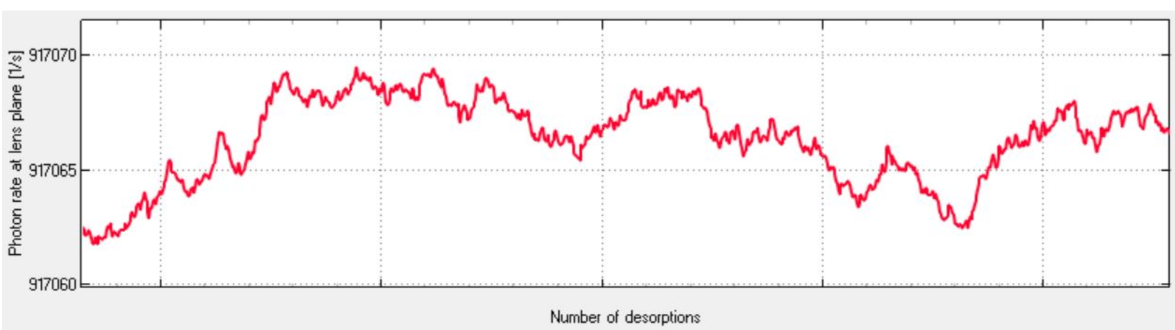

Figure 30: Convergence plotter example of spontaneous emission simulation. The graph shows the evolution of the photon rate at the lens plane (not scaled according to T_{total} (Equation 13)) during the emission of the last $3{\cdot}10^7$ emitted test photons.

The maximum and minimum of this graph can be used to estimate the accuracy of the simulation, independent from the simulation properties.
For the simulations involved in the results presented in Table 4, the uncertainty is well under 1 %. For test simulations in the following sections, the uncertainty is in the range of a couple percent.

In general, the effects of errors in the estimation of various simulation parameters are expected to exceed the inaccuracy of the MolFlow+ and SynRad+ algorithms by far and are therefore neglected in this stage of simulation.

7.2 Emission rates

As the behavior of the steady-state mode used in MolFlow+ as well as SynRad+ is linear, a change in emission rate results in the same change of the photon rate at the lens plane.

Spontaneous emission

One of the more significant sources of error in the calculation of the photon rate emitted by the interaction of the particle beams and the neon gas jet are the excitation cross sections, which are proportional to the photon rate (Equation 3.2.1). It is estimated, that due to the principle of equal velocities, electrons and protons "will give rise to the same excitation cross section" [43]. The lack of measured data in the range of 3 MeV to 7 TeV particle energy, leads to an extrapolation over one order of magnitude in case of the electron beam and six orders of magnitude for the proton beam, with a fit line described by a theoretical model [43]. For the proton beam, the result "may be affected by a large and hard to estimate error" [43].

According to the calculations, less than 1 % of the spontaneous emitted photons are generated by the proton-gas interaction. In a test simulation the source facet is scaled down to a corresponding proton beam width of $16.7\,\mu$m [51] with an emission rate of $3.9969\cdot10^6\,\mathrm{s}^{-1}$, leading to a photon rate with direct impact at the lens plane of about $1065\,\mathrm{s}^{-1}$ (after accounting for T_{total}). Therefore, the proton beam is harder to image and background radiation is an even bigger problem.

Thermal radiation

Due to the simplifications in section 4, regarding the calculation of emitted photons per second and in the selection of a source facet, the photon rate at the lens plane may be off by a few hundred percent. Even in the case of a photon rate, one order of magnitude higher than simulated, the thermal radiation background would be about 0.05 % of the signal's photon rate.
Therefore, the thermal radiation will be neglected in the further discussion.

Synchrotron radiation

Since the synchrotron radiation emission rate is calculated with SynRad+'s well tested algorithm and the High-Luminosity LHC beam properties as well as accurately measured magnetic properties as input, the expected error is negligible in comparison to the other simulations.

7.3 Reflection properties

In the following sections, the effect of deviations in the reflection properties will be discussed.

7.3.1 Reflectance

The reflectance values for the materials in Table 2 originate out of measurements, but are not necessarily applicable without any restrictions, as the materials used in the BGC might deviate from the ones used for the measurements.
When comparing multiple sources of reflectance measurements with the values chosen in Table 2, a deviation for copper towards higher reflectivities is noticeable. According to [52], the reflectance of copper is 70.1 % instead of the 61 % assumed in section 3.2.2. This matches with other sources shown in A.3.
As SynRad+ uses the reflectance table mentioned in section 2.6.2 and no copper parts are used in the MolFlow+ iteration of the synchrotron radiation, this deviation only affects the background photon rate of the spontaneous emission simulation.

A test simulation for the spontaneous emission case with a copper reflectance of 70 % shows less than 2 % more reflected photons at the lens plane. When increasing all reflectance values in this simulation by 10 % - a higher error than expected - the background photon rate would also rise 10 %, which is a small deviation in comparison to other sources of error shown in the following sections.

7.3.2 Specular and diffuse reflection

The reflection of rough surfaces in MolFlow+, modeled with a specular and diffuse part, is simpler than the one used in SynRad+, as it does not account for photon energy or

elevation angle.
The values for specular and diffuse reflection, of the materials used in the MolFlow+ simulations are roughly estimated. Only the values for stainless steel are based on a measurement, but with a material, which is probably smoother than the one used in the BGC, resulting in a higher amount of specular reflection. As the majority of photons, which are reflected onto the lens plane hit the steel port connecting the BGC's interaction chamber and camera arm, this part is of special interest regarding its reflection properties, like the ratio of specular and diffuse reflection.
To approximate the effects of a deviation in the ratio of specular and diffuse reflection, test simulations for the SE (Figure 31a) as well as the SR (Figure 31b) in MolFlow+ are made.
The magenta curves (square marks) of Figure 31 is generated by changing the specular and diffuse reflection properties of the facets resembling stainless steel. The teal curves (triangle marks) are generated by varying the properties of all facets except the stainless steel ones, where lens tubes and PVC bellow are assigned the same properties.

The graphs indicates that the photon rates at the lens plane are more reactive to a change of the stainless steel's specular and diffuse reflection, than to other materials. This can be derived from the higher gradients of the magenta curves - in comparison to the teal curves - describing a change in the stainless steel's properties.
This is expected, since the majority of background radiation in the SE and SR iteration simulation are reflected off of a stainless steel surface.

In contrast to Figure 31a, the SR photon rate at the lens plane (Figure 31b) is rising with an increasing part of diffuse reflection. An attempt to explain this can be made by interpreting the angular distribution of SE and SR at the facet of SR iteration inside the steel port (Figure 32).

In the SE case (Figure 32a), a lot of photons, which are reflected specular off of the stainless steel port, reach the lens plane. A deviation from that trajectory, caused by diffuse reflection, leads to more absorption in the low reflectance camera arm or reflection back to the interaction chamber.

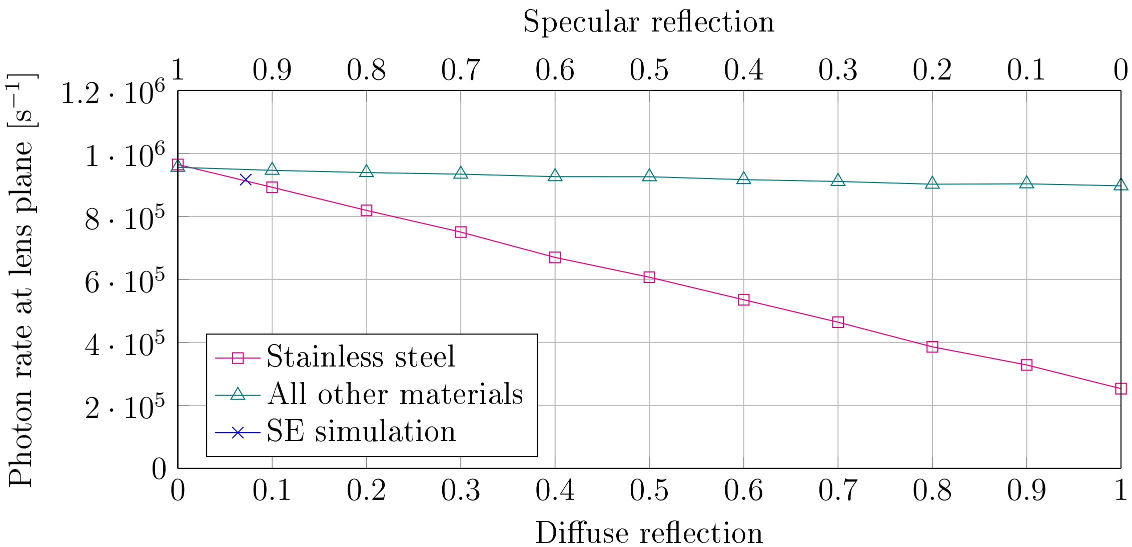

(a) Spontaneous emission photon rate at lens plane, dependent on specular and diffuse reflection.

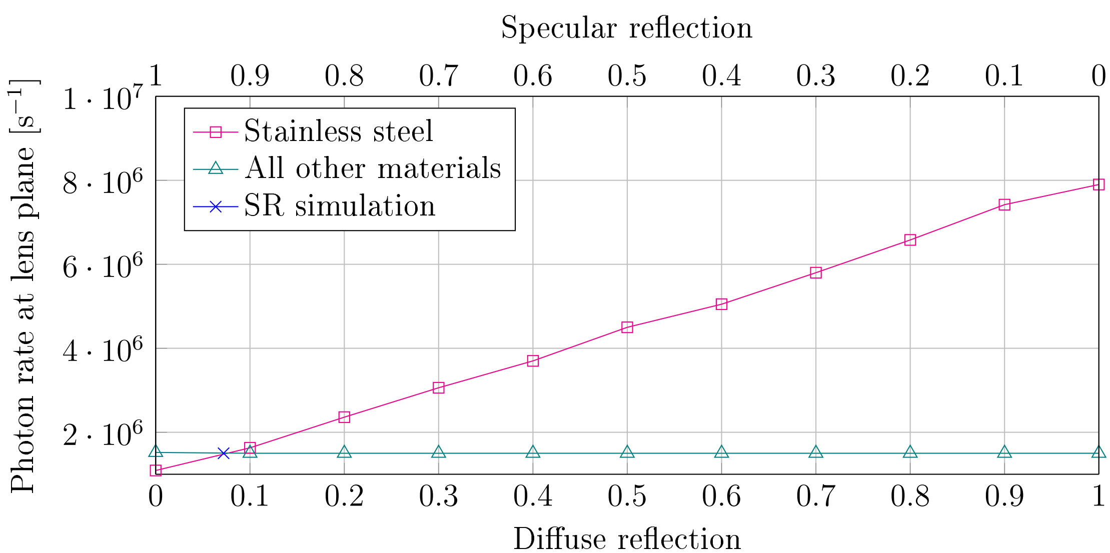

(b) Synchrotron radiation photon rate at lens plane, dependent on specular and diffuse reflection.

Figure 31: SE and SR photon rates at lens plane, dependent on specular and diffuse reflection. Magenta curves (square marks) are generated by changing the properties of stainless steel facets, teal curves (triangle marks) are generated by changing the properties of all facets expect the stainless steel ones.

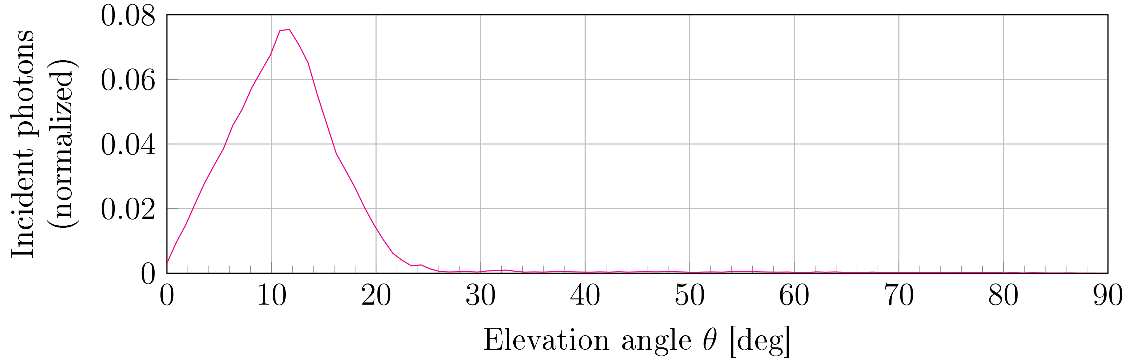

(a) Spontaneous emission angular profile at facet of SR iteration.

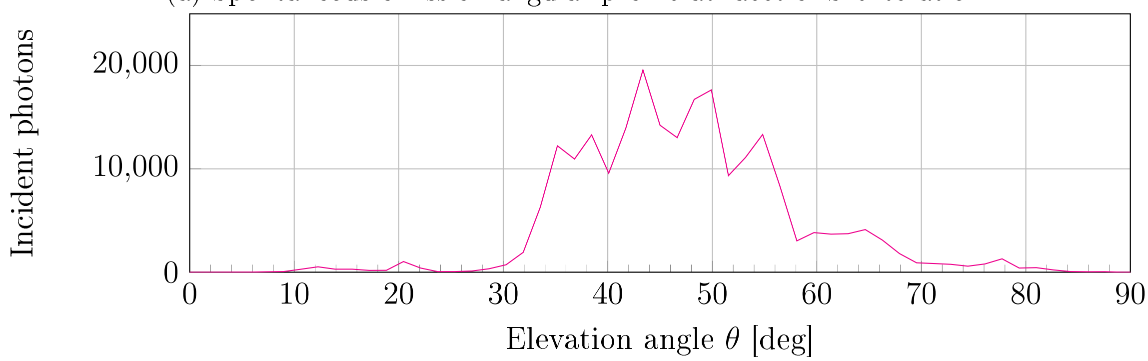

(b) Synchrotron radiation angular profile at facet of iteration.

Figure 32: Angular profiles of spontaneous emission (a) and synchrotron radiation (b) at facet of SR iteration.

The angular distribution of the SR at the facet of iteration (Figure 32b) is shifted to higher incident angles. Therefore, mainly the diffuse reflected part is able to reach the lens plane after reflection in the stainless steel port, causing higher photon rates for increasing diffuse reflection.

To verfify this thought, another simulation is made, where the camera arm is assigned a sticking factor of 1, to make sure the difference is due to the steel port. Thereby, only photons which hit the lens plane directly or are reflected off of the steel port can reach the lens plane.

Now, the angular profiles at the lens plane as well as at the end of the steel port towards the camera arm are recorded, while changing the ratio of specular to diffuse reflection from 0 to 1 (Figure 33).

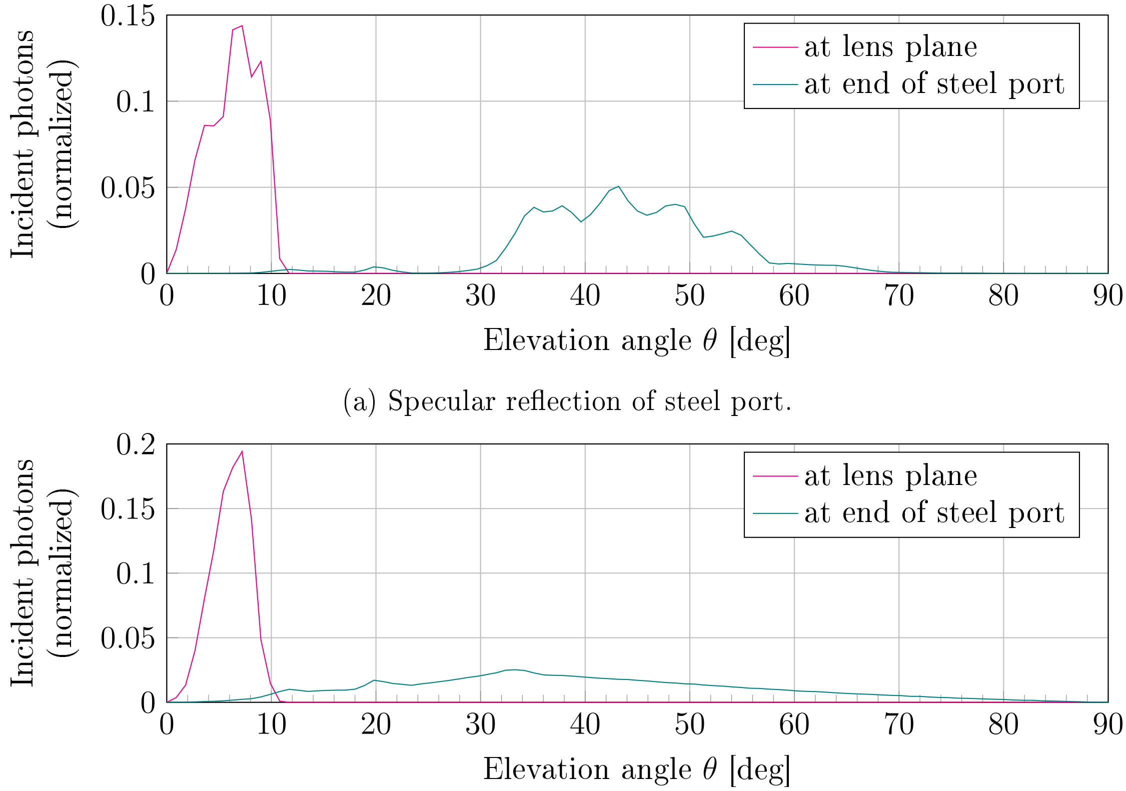

(a) Specular reflection of steel port.

(b) Diffuse reflection of steel port.

Figure 33: SR angular profiles with isolated specular (a) and diffuse (b) reflection at steel port and complete absorption in camera arm.

As the angular profile at the end of the steel port for diffuse reflection is significantly wider than for the specular reflection (teal curves in Figure 33), the amount of photons leaving the steel port with an elevation angle lower than 11° increases by a factor of about 7. This is consistent with the rise in photon rate at the lens plane with an increasing amount of diffuse reflection in the test simulation.

Overall, the background photon rate at the lens plane is expected to increase with higher diffuse reflection due to the higher gradient of the magenta curve for the synchrotron radiation (Figure 31b).

7.3.3 Roughness ratio

When changing the roughness ratio (RR) of the facets in the synchrotron radiation simulation in SynRad+, the photon rate at the facet of iteration changes (Figure 34).

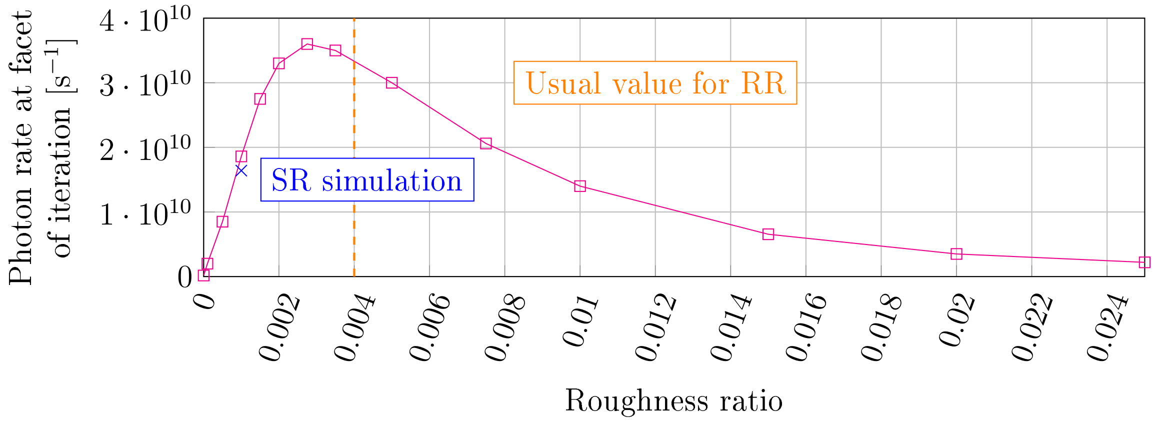

Figure 34: Photon rate at facet of SR iteration, dependent on roughness ratio. Blue data point (marked with an x) represents the SR simulation in SynRad+, with a roughness ration of 0.0005 for copper and 0.001 for all other materials.

When the roughness ratio was approximated in section 5.2, an error was made. The roughness ratio value usually varies around 0.004, the estimation in section 5.2 is therefore too low and according to Figure 34 an increase in the photon rate at the facet of SR iteration by a factor of 2 is possible, which would result in the same change in the lens plane photon rate.

7.4 Effect of iterative simulation

Due to the fact that the point of emission on a source facet is chosen randomly, there is an error in every iteration. If during the recording of an angle map, every photon is hitting the facet of recording in the same fraction of its surface area, when emitting according to this angle map, the points of emission are spread evenly across the surface. This effect is more present the bigger the facet of iteration is.

To estimate the error of an iteration, a test simulation is made, where the photon rate of spontaneous emission at the lens plane is measured with and without an iteration.

To keep the test close to the SR simulation, the same geometry including the facet of iteration is used and the angle map has similar parameters of 225716 hits sampled in 55 bins for the elevation angle over the whole azimuth range.

The simulation including the iteration shows about 26 % less photons at the lens plane in comparison to the simulation without an iteration.

7.5 Lens system and photon distribution at lens plane

The simulations are neither accounting for the lens system, nor the distribution of photons at the lens plane.
As Figure 35 shows, the photons at the lens plane representing the signal (Figure 35a) are distributed in a smaller area of the facet's center than the background photons (Figure 35b, 35c). The synchrotron radiation simulation is affected by the error of the iteration, including the neglected azimuth distribution, but the spread of photons on the lens plane is expected to be unaffected.

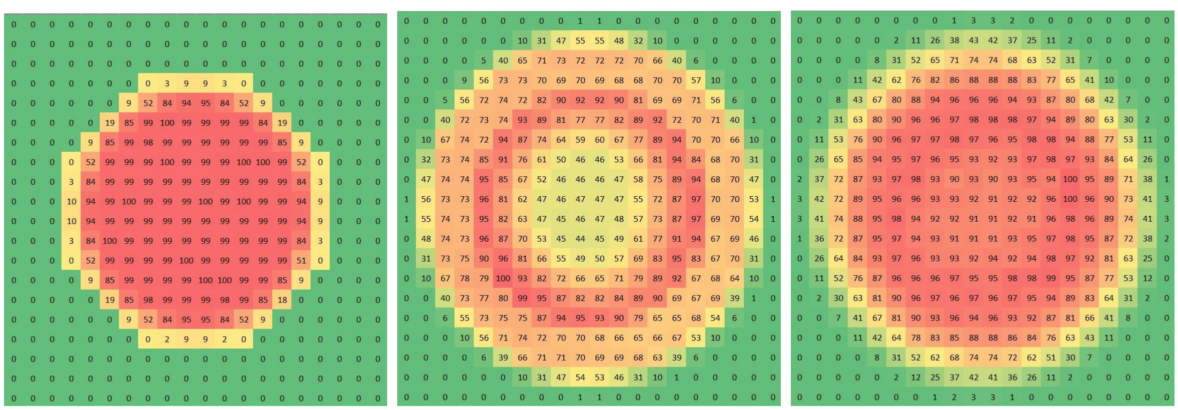

(a) SE signal (b) SE signal & background (c) SR background

Figure 35: Visualized photon distribution at the lens plane, values in each cell represent hits, normalized and in percent. (b) shows signal as well as background radiation of SE as the background can not easily be isolated.

Along with the refraction of the lens system, these two factors have an impact on how the camera system is processing the signal and their effect could be studied subsequently.

7.6 Recommendations

The next sections include recommendations for following actions as well as measures to verify the simulations and potentially lower the background photon rate at the lens plane.

7.6.1 Measurements of synchrotron radiation during run 3 of LHC

In reaction to these findings, the amount of synchrotron radiation could be measured at the place of installation, to verify the results of the simulation and if necessary, take precautions to reduce the amount of background radiation picked up by the BGC camera.
As a BGC prototype is already installed in IR4, during Run 3 of the LHC (proton experiments scheduled for mid-2022) [53] it could be used to take these preliminary measurements.

7.6.2 Mask in steel port

A mask in the steel port could be used to shield the camera from background photons. A test simulation is made, where a copper mask (reflection properties in Table 3.2.2) with a 13 mm ⌀ iris is incorporated into the lower part of the steel port (Figure 36).

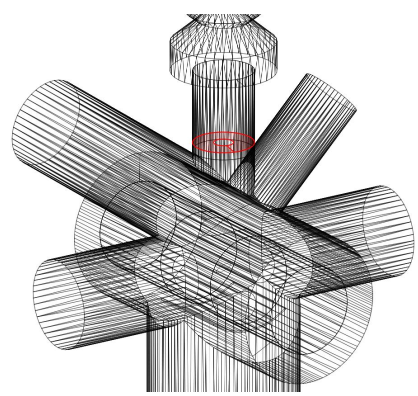

Figure 36: BGC interaction chamber with mask in steel port marked red.

Copper is used, as it is easy to fabricate with the tools at hand and the mask's material is not expected to have a great impact on the photon rate at the lens plane.

The simulation results with the mask in place are presented in Table 5 and visualized in Figure 37.

Table 5: Simulation results with mask in steel port and the photon rates at the lens plane differentiated according to signal and background; scaled according to the transmittance of the optical system.

Simulation	**Photon rate of emission** $[s^{-1}]$	**Photon rate at lens plane** $[s^{-1}]$	
Spontaneous emission	$5.72 \cdot 10^8$	signal	154679
		background	772
Synchrotron radiation	$2.26 \cdot 10^{15}$	background	81649

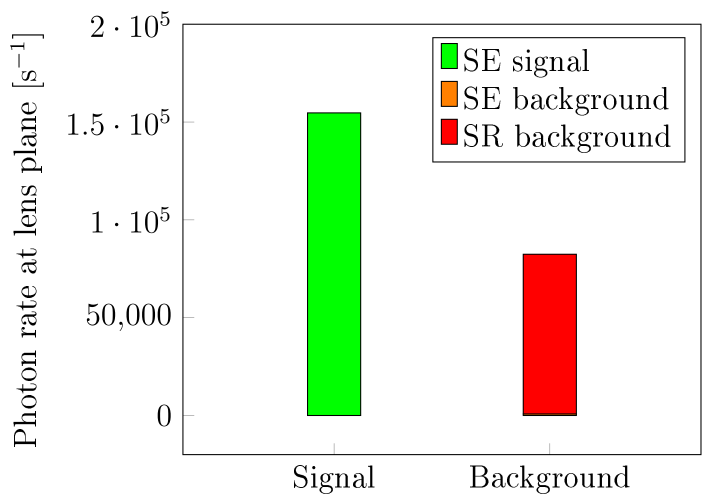

Figure 37: Visualized simulation results with mask in steel port.

From Table 5 the ratio of signal to background photons per second with a mask in the steel port X_{mask} is calculated as follows:

$$X_{mask} \approx \frac{154679\,\mathrm{s}^{-1}}{772\,\mathrm{s}^{-1} + 81649\,\mathrm{s}^{-1}} \approx 1.88$$

The signal to background ratio with a mask is about 17 times higher as the one presented in section 6.
The mask is able to remove over 99 % of background photons from the spontaneous emission, while letting over 99 % of the signal pass. At this point the deviation can solely be based on the fluctuation of the simulation result.
The SR result is greatly affected by the error of iteration, as the information of the photons position is lost with the iteration, which is crucial when simulating the effects of a mask. Nevertheless, a mask is expected to greatly improve the BGC's performance.

7.6.3 Black steel port

The data in Table 4 implies that - without a mask - about 75 % of photons coming from the spontaneous emission are reflected at least once before hitting the lens plane and therefore are background radiation. After further investigation, the port, which connects the BGC interaction chamber and the camera arm is responsible for about 80 % of the reflected light at the lens plane.
If the implementation of a mask in the steel port is not applicable or still a reasonable amount of photons are reflected off of the steel port, its reflectance could be decreased to reduce the photon rate at the camera.
As part of the interaction chamber is already AC-coated, the coating setup could be extended to include the steel port.

Test simulations for the SE and SR are made to estimate the background photon rates at the lens plane with a blackened steel port (Figure 38); the results are presented in Table 6 and visualized in Figure 39.

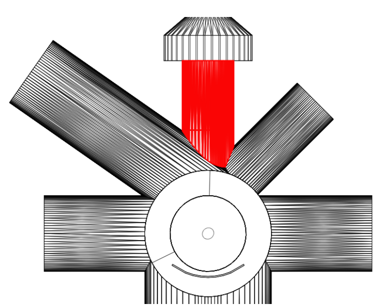

Figure 38: AC-coated parts in black port test simulations.

Table 6: Simulation results with black steel port and the photon rates at the lens plane differentiated according to signal and background; scaled according to the transmittance of the optical system.

Simulation	**Photon rate of emission** $[s^{-1}]$	**Photon rate at lens plane** $[s^{-1}]$	
Spontaneous emission	$5.72 \cdot 10^{8}$	signal	155103
		background	89346
Synchrotron radiation	$2.26 \cdot 10^{15}$	background	456059

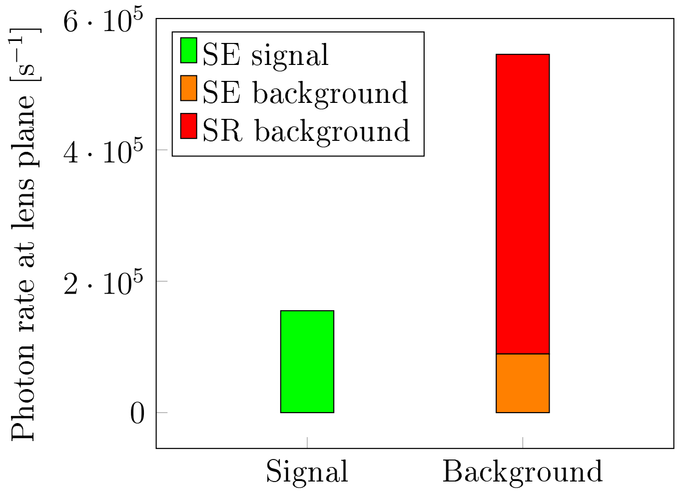

Figure 39: Visualized simulation results with blackened steel port.

From Table 6 the ratio of signal to background photons per second with a blackened steel port $X_{black-port}$ is calculated as follows:

$$X_{black-port} \approx \frac{155103\,\mathrm{s}^{-1}}{89346\,\mathrm{s}^{-1} + 456059\,\mathrm{s}^{-1}}$$
$$\approx 0.28$$

7.6.4 Saw-tooth profile to lower SR photon rate

A saw-tooth profile (Figure 40) on vacuum chambers is an efficient method to decrease the amount of forward scattered light. Photons hitting the part which is close to orthogonal in comparison to the photon direction, are more likely to be absorbed, as the scattering probability decreases with near-orthogonal incidence.

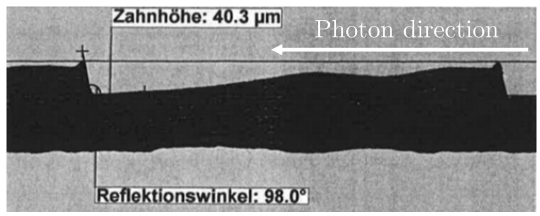

Figure 40: Microscopic surface view of saw-tooth profile incorporated in the LHC. Redrawn from [48].

To reduce the amount of synchrotron radiation at the lens plane, the part of the drift chambers between the BGC and magnet D4, which is exposed to the majority of direct incident photons could be changed to a saw-tooth profile (Figure 41).

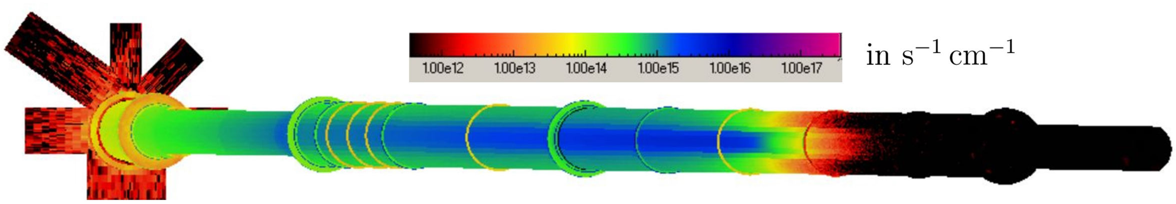

(a) Flux on synchrotron radiation geometry.

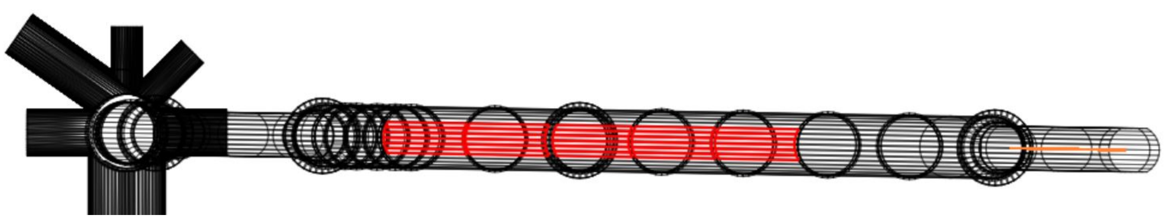

(b) Drift chamber facets with highest flux.

Figure 41: Synchrotron radiation simulation facets, which are suitable for saw-tooth machining.

8 Conclusion

This thesis aims to estimate the photon rates of different light sources, illuminating the camera of the Beam Gas Curtain instrument, developed in the course of the Large Hadron Collider's High Luminosity upgrade, by using Monte Carlo simulations.
They are able to give a rough estimation of the different light sources in the system. The synchrotron radiation can be identified as the biggest threat to the functionality of the BGC, especially considering a potential increase due to errors generated by the iteration as well as roughness ratio and the low signal photon rate expected from the proton-gas interaction. Meanwhile the thermal radiation of the electron gun cathode is very small in comparison to other background sources and therefore negligible.

In this stage, the simulations are not suited to give accurate predictions about real photon rates at the camera, as a lot of variables, like reflection properties or emission rates, are roughly estimated and the lens system is not accounted for.
The results are building a basis to understand the relation between the light sources and are valuable to identify potential threats and investigate subsequent steps and possible optimizations to reduce the background photon rate at the BGC monitor's camera, for example by incorporating a mask into the steel port, blackening it or partially applying saw-tooth machining to the drift chambers between the BGC and bending separator magnet D4.

A Appendices

The appendices deliver additional information as well as references about assumptions made throughout this thesis.

A.1 Materials

In the following, more information about the materials out of Table 3.2.2 and their reflection properties are provided.
If not stated otherwise, the ratio of specular and diffuse reflection is solely based on estimations, since no data is available.

Black anodized aluminum

The material encapsulating the lens system is made from anodized aluminum and fabricated by Thorlabs. The reflectance is obtained from Figure 42, made by Thorlabs.

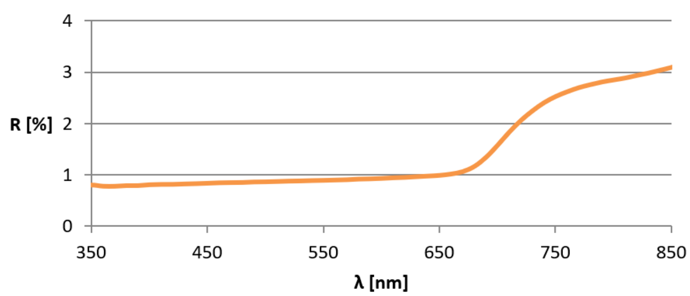

Figure 42: Spectral reflectance of black anodized aluminum for a 45° incident angle and an average of π and σ polarization.

Black PVC

The camera arm bellows are made out of black PVC and fabricated by RRG. Their reflectance is estimated on the basis of Figure 43 [54]. It does not include the reflectance at 585 nm, but it is estimated that the graph will follow the same gradient for shorter wavelengths.

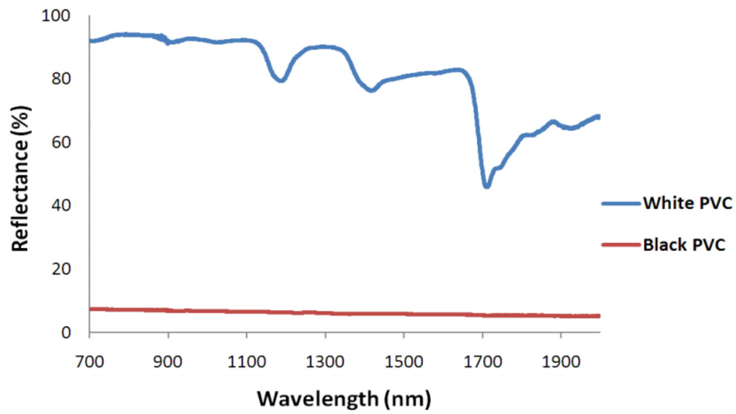

Figure 43: Spectral reflectance of black and white PVC [54].

Stainless steel

The vacuum chambers in the HEL and BGC are made out of stainless steel. The surface properties of the real parts are varying and could not be determined at the current stage of the project.
Thus, the reflectance at 584nm is taken from a technical report by NASA [52].
The ratio of specular and diffuse reflection is shown in Figure 44 [55]. The data is for a stainless steel surface with a mirror like finish, therefore the specular reflectance is high. As this is the only data available it is included into the MolFlow+ models and can be seen as a worst case approximation, since the photons can easier propagate long distances through the model (relevant in 4. The values in the graph are absolute, to insert them into MolFlow+ they have to be normalized.

Copper

The reflectance of copper is taken from Figure 45 [56].

AC-coating

The amorphous carbon coating was initially designed to reduce the problem of electron clouds in the LHC, induced by different effects responsible for the desorption of electrons from vacuum chambers [57].
Due to its low reflectance it is also used to absorb stray light in the BGC's RF liner. Its reflectance is taken from a presentation held at a BGC meeting at CERN [41].

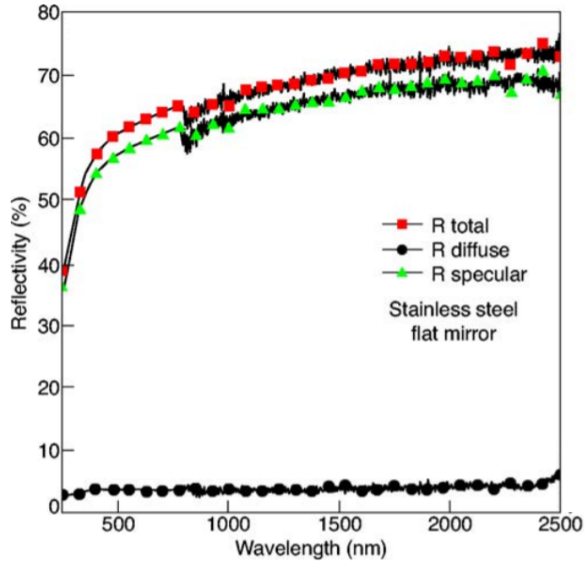

Figure 44: Total, specular and diffuse reflectance of a stainless steel mirror. Redrawn from [55].

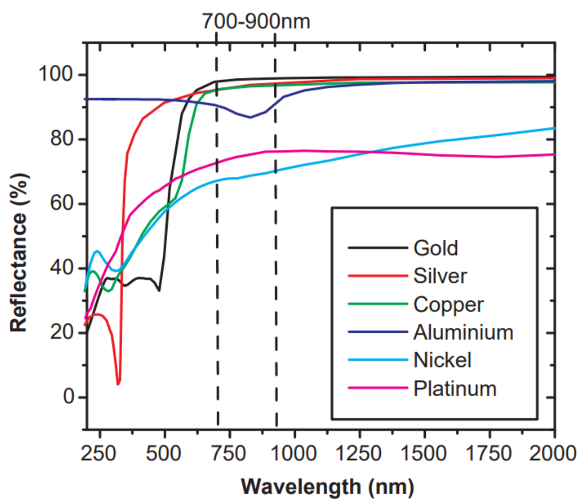

Figure 45: Spectral reflectance of different materials, including copper [56].

Polyteknik coating
Special coating process, which is used to provide a very low reflectance background for the camera.
Its reflectance is taken from a presentation held at a BGC meeting [41].

A.2 Vacuum view-port reflectance

Reflectance of Hositrad vacuum view-port between BGC camera arm and interaction chamber.

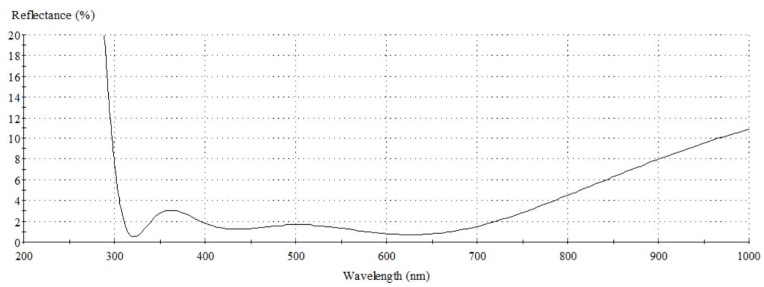

Figure 46: Spectral reflectance of vacuum view-port by Hositrad. Curve is not based on measurement, but calculations.

A.3 Copper reflectance

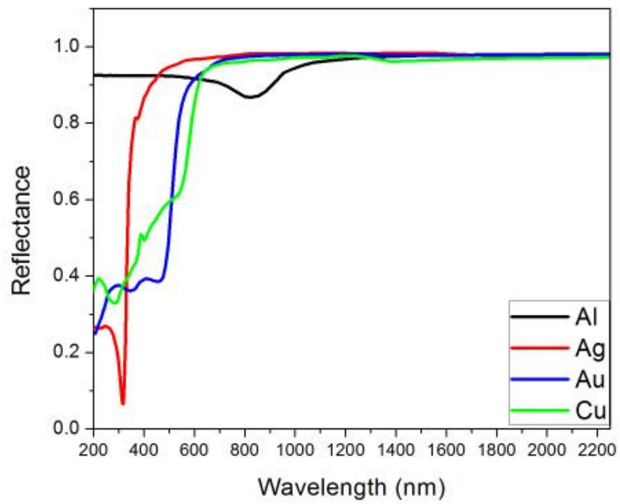

Figure 47: First alternative source for the spectral reflectance of copper [58]

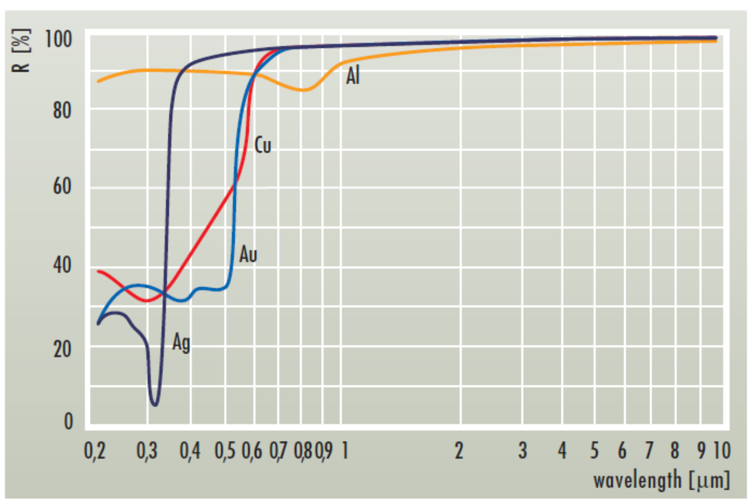

Figure 48: Second alternative source for the spectral reflectance of copper [59]

References

[1] Evans Lyndon and Bryant Philip. "LHC Machine". In: *Journal of Instrumentation* 3.08 (Aug. 2008). Accessed: 21.02.2021, S08001–S08001. DOI: {10.1088/1748-0221/3/08/s08001}. URL: https://doi.org/10.1088/1748-0221/3/08/s08001.

[2] Raymond Veness et al. "Development of a Beam-Gas Curtain Profile Monitor for the High Luminosity Upgrade of the LHC". In: (2019). Accessed: 25.03.2021, WEPB16. 5 p. DOI: 10.18429/JACoW-IBIC2018-WEPB16. URL: https://cds.cern.ch/record/2716030.

[3] Oscar Barbalat. "Applications of particle accelerators; rev. version". In: CERN-AC-93-04-BLIT-REV (Feb. 1994). Accessed: 21.02.2021, 23 p. DOI: 10.5170/CERN-1994-001.841. URL: https://cds.cern.ch/record/260280.

[4] Jorg Wenninger. "The LHC collider". In: *Comptes Rendus Physique* 16.4 (2015). Highlights of the LHC run 1 / Résultats marquants de la première période d'exploitation du GCH, Accessed: 21.02.2021, pp. 347–355. ISSN: 1631-0705. DOI: https://doi.org/10.1016/j.crhy.2015.03.005. URL: https://www.sciencedirect.com/science/article/pii/S1631070515000560.

[5] CERN. *The ATLAS detector*. https://atlas.cern/discover/detector. Accessed: 08.03.2021.

[6] CERN. *CMS detector*. https://cms.cern/detector. Accessed: 08.03.2021.

[7] CERN. *ALICE*. https://home.cern/science/experiments/alice. Accessed: 08.03.2021.

[8] CERN. *b is for beauty*. http://lhcb-public.web.cern.ch/en/Physics/Beauty-en.html. Accessed: 08.03.2021.

[9] CERN. *The Standard Model*. https://cds.cern.ch/record/1997201. Accessed: 03.03.2021. 2012.

[10] Nobel Media AB 2021. *The Nobel Prize in Physics 2013*. Press release. NobelPrize.org. https://www.nobelprize.org/uploads/2018/06/press-21.pdf. Accessed: 03.03.2021.

[11] "The European Strategy for Particle Physics Update 2013. La stratégie européenne pour la physique des particules Mise à jour 2013. 16th Session of European Strategy Council". In: (May 2013). Accessed: 03.03.2021. URL: https://cds.cern.ch/record/1567258.

[12] CERN. *A new schedule for the LHC and its successor*. https://home.cern/news/news/accelerators/new-schedule-lhc-and-its-successor. Accessed: 24.05.2021.

[13] Werner Herr and B Muratori. "Concept of luminosity". In: (2006). Accessed: 25.02.2021. DOI: 10.5170/CERN-2006-002.361. URL: https://cds.cern.ch/record/941318.

[14] I Béjar Alonso et al. *High-Luminosity Large Hadron Collider (HL-LHC): Technical design report*. Ed. by I Béjar Alonso. CERN Yellow Reports: Monographs. Accessed: 10.03.2021. Geneva: CERN, 2020. DOI: 10.23731/CYRM-2020-0010. URL: http://cds.cern.ch/record/2749422.

[15] L. Bottura. "Magnet Quench 101". In: arXiv:1401.3927 (Jan. 2014). Comments: 9 pages, Contribution to WAMSDO 2013: Workshop on Accelerator Magnet, Superconductor, Design and Optimization; 15 - 16 Jan 2013, CERN, Geneva, Switzerland, Accessed: 10.03.2021, 1–9. 9 p. DOI: 10.5170/CERN-2013-006.1. URL: https://cds.cern.ch/record/1643429.

[16] D Mirarchi et al. "Hollow electron-lens assisted collimation and plans for the LHC". In: FERMILAB-CONF-18-311-AD-APC (2018). Accessed: 12.03.2021. DOI: 10.18429/JACoW-HB2018-TUP1WE02. URL: https://cds.cern.ch/record/2640825.

[17] Gulio Stancari. *Hollow electron beam collimation for the LHC upgrade, Fermi National Accelerator Laboratory*. LHC Collimation Upgrade Specification Meeting, http://lhc-collimation-upgrade-spec.web.cern.ch/Files/meetings/30/GStancari_ColUSM_131018.pdf. Accessed: 20.03.2021. Oct. 2013.

[18] Stefano Redaelli et al. "Plans for deployment of hollow electron lenses at the LHC for enhanced beam collimation". In: (2015), 4 p. URL: https://cds.cern.ch/record/2025002.

[19] R. Wanzenberg. *Impedances and Instabilities*. https://arxiv.org/pdf/2006.06540.pdf. Accessed: 23.04.2021. 2020. arXiv: 2006.06540 [physics.acc-ph].

[20] Diego Perini and Carlo Zanoni. *Preliminary Design Study of the Hollow Electron Lens for LHC*. Tech. rep. CERN-ACC-NOTE-2017-0004. Accessed: 12.03.2021. Geneva: CERN, Jan. 2017. URL: https://cds.cern.ch/record/2242211.

[21] Tom Marriott-Dodington. *A Beam Gas Curtain Monitor for HL-LHC, CERN BI Day 2018*. https://indico.cern.ch/event/764999/contributions/3179137/attachments/1764591/2864235/A_Beam_Gas_Curtain_Monitor_for_HL-LHC_TMD.pdf. Dec. 2018.

[22] Dieter Meschede. "Gerthsen Physik". In: 24th ed. Springer-Lehrbuch. Springer-Verlag Berlin Heidelberg, 2010, p. 604.

[23] Serban Udrea and Peter Forck. *Milestone 1.4 Report*. CERN e-Lens Project, Accesssed: 02.04.2021. GSI Helmholtzzentrum für Schwerionenforschung, Sept. 2017. URL: https://edms.cern.ch/ui/#!master/navigator/document?D:100580523:100580523:subDocs.

[24] Ekbert Hering, Rolf Martin, and Martin Stohrer. "Physik für Ingenieure". In: 9th ed. Springer-Lehrbuch. Springer-Verlag Berlin Heidelberg, 2004, pp. 520–524.

[25] Horst Kuchling. "Taschenbuch der Physik". In: 20th ed. Hanser Fachbuchverlag, 2011, pp. 553–554.

[26] Dieter Meschede. "Gerthsen Physik". In: 25th ed. Springer-Lehrbuch. Springer-Verlag Berlin Heidelberg, 2015, p. 777.

[27] Dieter Meschede. "Gerthsen Physik". In: 24th ed. Springer-Lehrbuch. Springer-Verlag Berlin Heidelberg, 2010, p. 295.

[28] Universität Ulm. *Strahlung des schwarzen Körpers*. https://www.uni-ulm.de/fileadmin/website_uni_ulm/nawi.inst.251/Didactics/quantenchemie/html/schwK-F.html. Accessed: 29.03.2021.

[29] Ekbert Hering, Rolf Martin, and Martin Stohrer. "Physik für Ingenieure". In: 11th ed. Springer-Lehrbuch. Springer-Verlag Berlin Heidelberg, 2012, pp. 258–261.

[30] Brandenburgische technische Universität. *Plancksches Strahlungsgesetz*. https://www-docs.b-tu.de/ag-festkoerperphysik/public/w4.pdf. Accessed: 30.03.2021.

[31] Stephen Scopatz et al. "Comparison of emissivity evaluation methods for infrared sources, Proceedings of SPIE - The International Society for Optical Engineering". In: (2009). Accessed: 31.03.2021. URL: physics.ucf.edu/~ishigami/Teaching/Phys4083L/lab%20descriptions/NETD/Comparison%20of%20Emissivity%20Evaluation%20Methods%20for%20Infrared%20Sources.pdf.

[32] Helmut Wiedemann. "Particle accelerator physics". In: 4th ed. Berlin: Springer, 2015, p. 800.

[33] Helmut Wiedemann. "Particle accelerator physics". In: 4th ed. Berlin: Springer, 2015, pp. 816–817.

[34] Helmut Wiedemann. "Particle accelerator physics". In: 4th ed. Berlin: Springer, 2015, p. 837.

[35] Marton Ady. "MolFlow 2.6 algorithm". In: (Mar. 2016). Accessed: 05.04.2021. URL: https://molflow.web.cern.ch/sites/molflow.web.cern.ch/files/molflow_docu.pdf.

[36] Peter Bonate. "A Brief Introduction to Monte Carlo Simulation". In: *Clinical pharmacokinetics* 40 (Feb. 2001). DOI: 10.2165/00003088-200140010-00002. URL: https://www.researchgate.net/publication/12094719_A_Brief_Introduction_to_Monte_Carlo_Simulation.

[37] Marton Ady. "Synrad 1.4 algorithm". In: (Mar. 2016). Accessed: 14.04.2021. URL: https://molflow.web.cern.ch/sites/molflow.web.cern.ch/files/synrad_docu.pdf.

[38] G. Palasantzas and J.Th.M. de Hosson. "Wetting on rough surfaces". In: *Acta Materialia* 49.17 (2001). Accessed: 15.04.2021, pp. 3533–3538. ISSN: 1359-6454. DOI: https://doi.org/10.1016/S1359-6454(01)00238-5. URL: https://www.sciencedirect.com/science/article/pii/S1359645401002385.

[39] CERN. *OpticsBuilder documentation*. https://molflow.web.cern.ch/content/opticsbuilder-documentation. Accessed: 15.04.2021.

[40] Guido Sterbini. *Introduction to MAD-X*. https://molflow.web.cern.ch/content/opticsbuilder-documentation. CERN accelerator school, Accessed: 15.04.2021. Jan. 2014.

[41] Marton Ady. *SR simulation first results*. https://edms.cern.ch/ui/#!master/navigator/document?D:100778308:100778308:subDocs. BGC meeting, Accessed: 23.04.2021. Apr. 2019.

[42] Adriana Rossi and Sergey Sadovich. *HEL test stand update*. https://indico.cern.ch/event/879781/?print=1. BGC collaboration meeting, Accessed: 21.04.2021. Mar. 2020.

[43] Serban Udrea and Peter Forck. *Milestone 1.1 Report*. CERN e-Lens Project, Accesssed: 21.04.2021. GSI Helmholtzzentrum für Schwerionenforschung, Sept. 2018. URL: https://edms.cern.ch/ui/#!master/navigator/document?D:100580521:100580521:subDocs.

[44] Apollinari, G. and Brüning, O. and Nakamoto, T. and Rossi, Lucio. "High Luminosity Large Hadron Collider HL-LHC". In: (2015). Accessed: 21.04.2021. DOI: 10.5170/CERN-2015-005.1. arXiv: 1705.08830 [physics.acc-ph]. URL: https://inspirehep.net/literature/1601167.

[45] Ondrej Sedlacek. "simulation of electron beam transport within hollow electron lens using warp and development of calibration method for beam loss monitors". Accessed: 21.04.2021. Oct. 2020. URL: https://cds.cern.ch/record/2749934.

[46] TRANSMETRA. *TABLE OF EMISSIVITY OF VARIOUS SURFACES*. https://www.transmetra.ch/images/transmetra_pdf/publikationen_literatur/pyrometrie-thermografie/emissivity_table.pdf. Accessed: 30.04.2021.

[47] B. Angerth et al. "The LHC beam screen: Specification and design". In: *4th European Particle Accelerator Conference* (1995). Accessed: 07.05.2021. URL: %5Curl%7Bhttps://accelconf.web.cern.ch/e94/PDF/EPAC1994_0208.PDF%7D.

[48] Marton Ady. "Monte Carlo simulations of ultra high vacuum and synchrotron radiation for particle accelerators". May 2016. URL: https://cds.cern.ch/record/2157666.

[49] H Burkhardt. *Monte Carlo generation of the energy spectrum of synchrotron radiation*. Tech. rep. Geneva: CERN, June 2007. URL: http://cds.cern.ch/record/1038899.

[50] G. F. Dugan et al. "Measurements of x-ray scattering from accelerator vacuum chamber surfaces, and comparison with an analytical model". In: *Physical Review Accelerators and Beams* 18.4 (Apr. 2015). Accessed: 03.06.2021. DOI: 10.1103/PhysRevSTAB.18.040704. URL: https://ui.adsabs.harvard.edu/abs/2015PhRvS..18d0704D.

[51] L Rossi and O Brüning. "Introduction to the HL-LHC Project". In: *Adv. Ser. Dir. High Energy Phys.* 24 (2015). Accessed: 15.06.2021, pp. 1–17. DOI: 10.1142/9789814675475_0001. URL: https://cds.cern.ch/record/2130736.

[52] Ernie Spisz et al. *SOLAR ABSORPTANCES AND SPECTRAL REFLECTANCES OF 12 METALS FOR TEMPERATURES RANGING FROM 300 TO 500 K.* Tech. rep. Accessed: 22.04.2021. Cleveland, Ohio, USA: NASA, Aug. 1969. URL: https://www.osti.gov/biblio/5248661.

[53] CERN. *Longer term LHC schedule.* https://lhc-commissioning.web.cern.ch/schedule/LHC-long-term.htm. Accessed: 29.05.2021.

[54] Hamed Masoumi, Seyed Mohsen Safavi, and Z. Khani. "Identification and classification of plastic resins using near infrared reflectance spectroscopy". In: *International Journal of Mechanical and Industrial Engineering* 6 (Jan. 2012). Accessed: 22.04.2021, pp. 213–220. URL: %5Curl%7Bhttps://www.researchgate.net/publication/285330830_Identification_and_classification_of_plastic_resins_using_near_infrared_reflectance_spectroscopy%7D.

[55] M. Rubel et al. "Mirror test for International Thermonuclear Experimental Reactor at the JET tokamak: An overview of the program". In: *Review of Scientific Instruments* 77 (June 2006). Accessed: 22.04.2021. DOI: 10.1063/1.2202915. URL: https://www.researchgate.net/publication/37459596_Mirror_test_for_International_Thermonuclear_Experimental_Reactor_at_the_JET_tokamak_An_overview_of_the_program.

[56] Bin Wang and Laurent Gallais. "A theoretical investigation of the laser damage threshold of metal multi-dielectric mirrors for high power ultrashort applications". In: *Opt. Express* 21.12 (June 2013). Accessed: 21.04.2021, 14698–14711. DOI: {10.1364/OE.21.014698}. URL: %7Bhttp://www.opticsexpress.org/abstract.cfm?URI=oe-21-12-14698%7D.

[57] C Yin Vallgren et al. *Recent Experimental Results on Amorphous Carbon Coatings for Electron Cloud Mitigation*. Tech. rep. Accessed: 23.04.2021. Geneva: CERN, Oct. 2011. URL: http://cds.cern.ch/record/1387885.

[58] Andressa Dancini Goncalves. *Metallic Reflection*. https://eng.libretexts.org/Bookshelves/Materials_Science/Supplemental_Modules_(Materials_Science)/Optical_Properties/Metallic_Reflection. Accessed: 14.06.2021.

[59] LAYERTEC. *Metallic Coatings*. https://www.layertec.de/en/capabilities/coatings/metallic/. Accessed: 14.06.2021.